UNIVERSITY OF OKLAHOMA GRADUATE COLLAGE

EXPERIMENTAL INVESTIGATION AND CHARACTERIZATION OF TURBULENT SPOTS ON A WEDGE IN A HYPERSONIC BOUNDARY LAYER

A THESIS

SUBMITTED TO THE GRADUATE FACULTY

in partial fulfillment of the requirements for the

Degree of

MASTER OF SCIENCE

By

KOSUKE YOSHIKAWA

Norman, Oklahoma

2024

EXPERIMENTAL INVESTIGATION AND CHARACTERIZATION OF TURBULENT SPOTS ON A WEDGE IN A HYPERSONIC BOUNDARY LAYER

A THESIS APPROVED FOR THE

SCHOOL OF AEROSPACE AND MECHANICAL ENGINEERING

BY THE COMMITTEE CONSISTING OF

Dr. Hiroshi Ozawa, Chair

Dr. Prakash Vedula

Dr. Ramkumar Parthasarathy

Acknowledgments

I would like to acknowledge my supervisor, Dr. Ozawa. All the communications, discussions, and instruction during my time in the High-Speed Aerothermodynamics Laboratory (HSAL) were helpful and fruitful.

I also thank the people I communicated with during the Master's program. The machining shop staff, Billy and Greg, gave advice and helped me do some machining in the shop. The students in the HSAL, Michael, Nick, and Ryo, gave me lots of comments and discussions regarding the research.

Finally, I deeply appreciate my family. Without their help, I would never be able to study here at the University of Oklahoma, and this work would never be completed.

Table of Contents

List of Figures

List of Tables

Abstract

The Boundary Layer Transition (BLT) is a serious problem for high-speed vehicles since a vehicle experiences a huge thermal load during a hypersonic flight. Especially, the thermal load becomes so significant that it may destroy the vehicle by altering and/or melting the surface structure in the BLT region. Therefore, it is essential to predict the location of BLT for designing hypersonic vehicles. BLT has been investigated for several decades. Previous experimental and theoretical investigations indicated that the merging of turbulent spots results in a fully developed turbulent boundary layer. Therefore, it is important to study the characteristics of turbulent spots for a better understanding and accurate prediction of BLT location. In this study, the boundary layer flow on a wedge model was investigated using pressure sensors, and turbulent spots were visualized by measuring the heat flux on the surface of a wedge model using a fast-response Temperature-Sensitive Paint (TSP). The frequency analysis may indicate the boundary layer flow was transitional. The global heat flux distribution derived by TSP measurements visualized turbulent spots propagating downstream. Based on the global heat flux distribution, the propagation velocity, the peak heat flux, the lateral spreading angle, the vertex angle, and the number of turbulent spots that appeared during test durations were obtained. Some of the results show good agreement with data available in the previous research, showing the ability of the TSP used in this study.

1. Introduction

The Boundary Layer Transition (BLT) process affects many aerothermodynamic parameters such as surface pressure and skin friction [1]. In hypersonic flights, when the BLT occurs, surface heat transfer significantly increases [2]. Therefore, it is essential to accurately predict the location of the onset and the extent of the BLT region in the design of hypersonic vehicles to protect the vehicle from the thermal load. For more than half a century, experimental, theoretical, and numerical studies regarding the BLT have been done [3-6]. Kendall [3] studied the growth of natural fluctuations in the boundary layer flow on a flat plate and a cone using hot-wire anemometry in various Mach number flows and found that fluctuation growth started ahead of the location where the growth of pressure fluctuation was expected to become important. Grossir et al. [4] performed experiments using a cone model with different nose radii and observed the behavior of the instability waves. Mack [5] theoretically studied the linear stability theory and calculated the effects of freestream Mach number on the BLT, and concluded that the variation of transition Reynolds number (Re) with mean-flow parameter and transition Re depends on what happens where the linear stability theory was valid. Sivasubramanian and Fasel [6] carried out a Direct Numerical Simulation (DNS) to investigate the transition mechanism on a cone with a half angle of 7° in a Mach 6 flow and the results indicated that the fundamental breakdown of the second mode waves may play a role in natural unforced BLT. These studies indicated that the second mode instability waves are relevant to the hypersonic BLT. The instability waves, that were introduced by the receptivity mechanism [7, 8], are amplified in the boundary layer and eventually breakdown to generate turbulent spots in small disturbance environments. In some scenarios, turbulent spots are directly made by the freestream disturbances in the bypass mechanisms in a large disturbance environment [9].

Notably, because the turbulent boundary layer is formed by the merging of turbulent spots [10, 11], it is also important to study the characteristics of turbulent spots. Since when Emmons [12] observed the turbulent spots in water table experiments, many experimental investigations regarding turbulent spots have been made for more than half a century [10, 11, 13-17]. Some numerical studies have also been performed to investigate the characteristics of turbulent spots [18, 19]. The common results found in these investigations are mainly (1) turbulent spots propagate at a fraction of boundary layer edge velocity and (2) turbulent spots stretch in span- and streamwise directions during propagation. Despite that a number of investigations have been done, however, it cannot be said that the characteristics of turbulent spots have fully been understood. Additionally, in many of these experimental studies, intrusive techniques were used for the measurements, such as hot-wire anemometry, thermocouples, and thin-film gauges. Since the intrusive way may alter the flowfield, non-intrusive measurements are desired.

One of the non-intrusive methods is taking photographs. Demetriades [20] used the Schlieren visualization to investigate the boundary layer flow on a cone and successfully captured the rope-like structure. James [21] used the shadowgraph technique in a gun-tunnel facility and captured some turbulent spots propagating on free-flight objects. Laurence et al. [22] utilized the high-speed Schlieren visualization technique to study instability waves in a hypersonic boundary layer on a cone. Butler and Laurence [23] investigated the behavior of the instability waves in a boundary layer on a cone-flare configuration using high-speed Schlieren visualization. In these studies, turbulent spots and instability waves were recorded and characterized quantitatively, showing the ability of optical measurement techniques, such as Schlieren and shadowgraph visualization.

Another optical technique to study BLT and turbulent spots is Temperature-Sensitive Paint (TSP) [24]. To obtain the global information from pointwise measurements, the probes must be mounted sufficiently dense for interpolation and it may result in a high implementation cost. On the contrary, TSP can be applied cheaply to the surface of interest and can provide global temperature and heat flux distribution since one luminescent molecule acts as a temperature sensor. In recent years, supersonic and hypersonic BLT have been studied using TSP techniques [25,26]. Ozawa et al. [25] applied a fast-response TSP on a cone with a 7° half-angle cone and obtained heat flux distribution in a Mach 7.4 flow in the High Enthalpy Shock Tunnel Göttingen (HEG) of the German Aerospace Center (DLR). Laurence et al. [26] investigated the heat flux distribution on an inlet ramp model and observed BLT. Moreover, Ozawa [27] investigated the aerothermodynamic phenomena on a shock tube wall using a fast-response TSP and obtained quantitative results with high spatial and temporal resolutions. These experimental studies showed that the TSP can be a good option to investigate BLT in high-speed flows.

This study aims to investigate and characterize the turbulent spots in hypersonic boundary layers by measuring the heat flux on the surface of the test model with a high spatial- and temporal resolution using a fast-response TSP. Alongside the TSP measurement, pressure transducers were used to record the pressure and pressure fluctuation during the tests.

2. Experimental Facility and Measurement Techniques

2.1 Experimental Facility and Test Condition

All the experiments were performed using the reflected shock tunnel facility at the University of Oklahoma (OU). The schematic of the shock tunnel is given in Figure 1. The shock tunnel facility consisted of four parts, namely, driver tube, shock tube, nozzle, and test section. The initial condition for the driver tube and shock tube are presented in Table 1 together with the nominal shock speed and corresponding shock Mach number. The behavior of the waves inside the shock tube section is shown as an *x-t* diagram in Figure 2. At the moment the fast valve, located between the driver tube and the shock tube, opens the incident shock wave is formed and propagates downstream and is reflected at the endwall at a later time. Following the incident shock wave, the contact surface, the interface between the gases that were in the driver tube and the shock tube, propagates in the shock tube towards the endwall. The reflected shock wave, propagating upstream interacts with the contact surface at some point. Under the

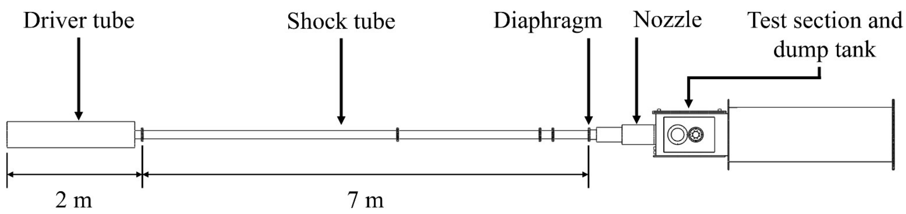

Figure 1 Shock tunnel facility

Table 1 Initial condition and nominal shock speed and shock Mach number for shock tube

p_4 (MPa)	p_1 (kPa)	u_s (m/s)	M_s
3.1	36	730	2.08

over-tailored condition, the contact surface keeps propagating downstream toward the endwall after the interaction with the reflected shock wave. After several reflections, the contact surface eventually reaches the endwall of the shock tube. For the shock tunnel, the gas near the endwall is used as the reservoir for the freestream in the test section. The temperature of the reservoir gas is kept high from the time the incident shock wave reaches the endwall to the time the contact surface arrives at the endwall. Corresponding to the contact surface arrival at the endwall, the temperature of the reservoir gas starts decreasing and is stabilized. The reservoir condition is kept until the expansion wave arrives at the endwall. Due to the change in the reservoir condition, the freestream condition changes over time. In the case of the shock tunnel facility used in the study, when the incident shock arrives at the end of the shock tube section, the diaphragm, which is located between the shock tube and the nozzle, ruptured instantaneously to generate Mach 5.2 flow in the test section through an isentropic expansion

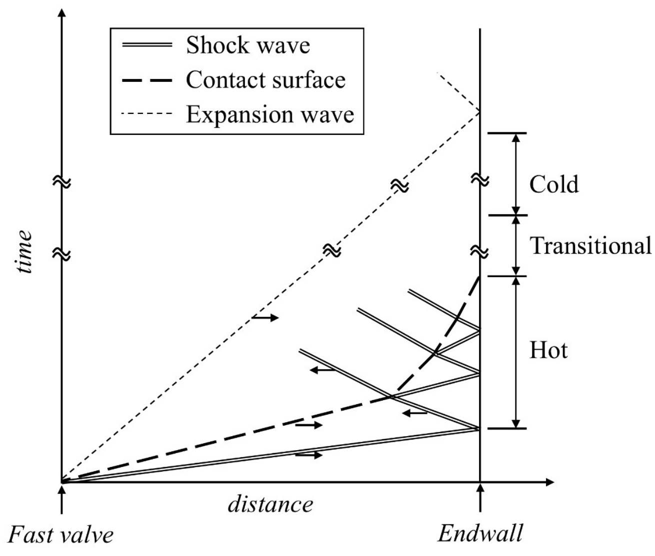

Figure 2 The *x-t* diagram of waves inside a shock tube. Arrows show the direction of wave propagation

in the nozzle. The exit diameter of the nozzle was 200 mm. The test section had two optical windows for optical measurements.

In this study, the test condition tabulated in Table 2 was employed so that the boundary layer flow on the wedge becomes transitional. The typical pressure variation in the reservoir and at the stagnation point in the test section is shown in Figure 3 together with the heat flux and temperature variation at the stagnation point in the test section. The temperature and heat flux variation at the stagnation point in the test section was measured using a hemisphere model

Table 2 Reservoir and freestream conditions

	Hot gas condition	Cold gas condition
p_0 (kPa)	1430	1580
M_∞	5.2	5.2
T_∞ (K)	130	50
p_∞ (kPa)	2.1	2.4
ρ_∞ (kg/m^3)	0.056	0.16
u_∞ (m/s)	1200	739
Re_∞ $\times 10^6$ (1/m)	7.4	38

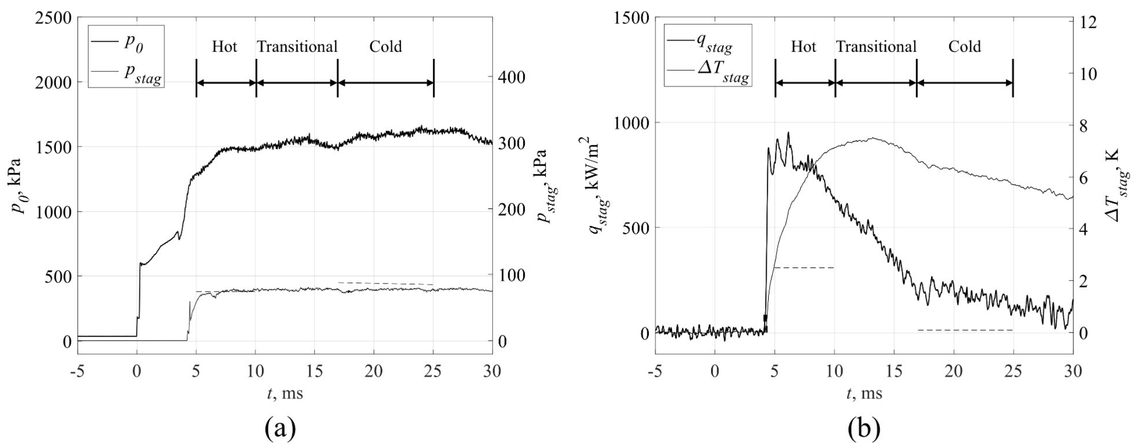

Figure 3 Time history of (a) pressure in the reservoir and stagnation point in the test section and (b) temperature variation and heat flux at the stagnation in the test section. Dashed lines show theoretically estimated values

equipped with a type-E thermocouple. Since dried air was used as the driver and test gases, the shock tunnel was operated under the over-tailored condition. As mentioned earlier, when the contact surface arrives at the reservoir, the temperature of the reservoir gas decreases and the density increases, resulting in a drastic increment in the unit Re in the freestream condition. Immediately after the flow started, the heat flux at the stagnation point was kept at approximately q=790 kW/m^2 and then it gradually decreased and was kept at approximately q=180 kW/m^2 in later time. Each time region was defined as hot-, transitional-, and cold gas conditions as denoted in Figure 3. The calculation of experimental and theoretical heat flux at the stagnation point will be discussed shortly. For the hot- and cold gas conditions, the reservoir condition was theoretically calculated using the initial condition and incident shock Mach number, M_s. The freestream condition was calculated using the reservoir gas condition and freestream Mach number, M_∞.

2.2 Test Model

The test model was a wedge made of aluminum. The schematic is shown in Figure 4 together with dimensions. The width and length of the wedge were 150 mm and 230 mm. Two acrylic plates were attached on both sides of the wedge to mitigate the three-dimensional effect on the boundary layer growing on the surface. A White Polyurethane paint (WP) was applied on the surface to make TSP measurements. The thickness of the WP layer was approximately

0.5 mm and the surface was smooth such that light was reflected. The radius of the leading edge of the wedge was measured to be less than 0.5 mm after the application of the WP. Because the surface of interest was inclined 7.4 degrees to the freestream, an oblique shock wave was generated at the leading edge of the wedge. An instantaneous Schlieren image taken in a test duration and the time-averaged Schlieren image are shown in Figure 5. The oblique shock wave angle was measured to be 17.6˚ by fitting a line to the oblique shock wave in a time-averaged image as shown in Figure 5(b). The post-oblique shock wave condition was calculated based on the oblique shock wave angle generated at the leading edge of the wedge and freestream condition using the oblique shock relationship, and presented in Table 3. Pressure sensors were mounted on the wedge to measure the static pressure and pressure fluctuation due to the

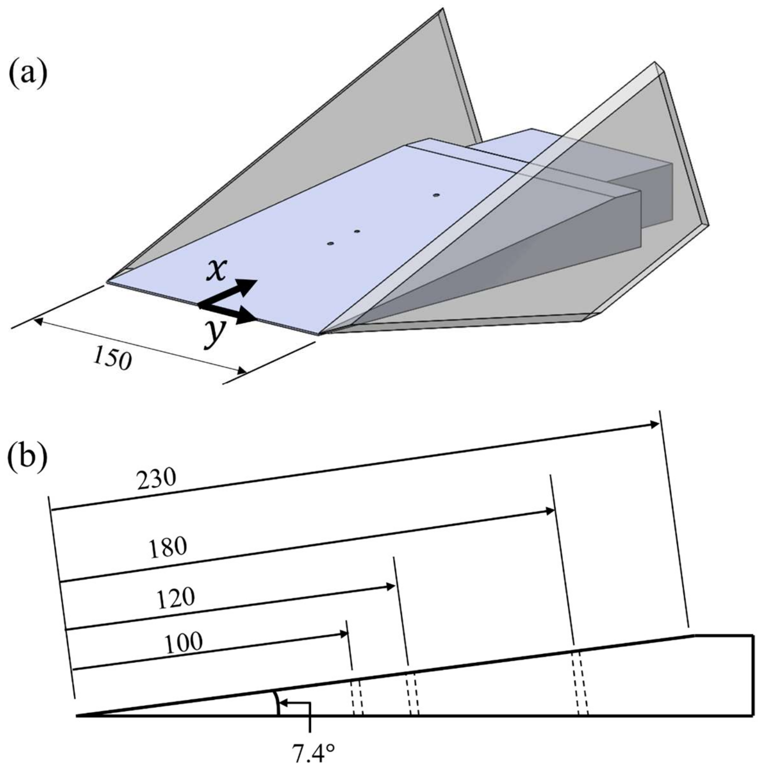

Figure 4 Wedge model. (a) 3D Sketch and (b) side view. Dimensions are in mm

instability waves. More will be addressed in the later section.

2.3 Measurement Techniques

2.3.1 Thermocouple

A type-E thermocouple (TC) was used to measure the temperature variation at the stagnation point in the test section. From the temperature variation, the heat flux was calculated using the method proposed by Cook and Felderman [28]. The discretized form of the method is shown

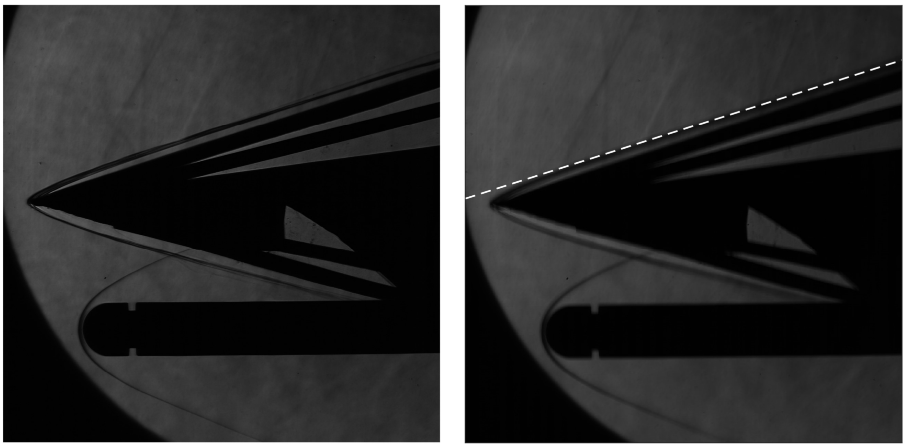

(a) (b)

Figure 5 Schlieren images taken in the test duration. (a) Instantaneous image and (b) time-averaged image. Dashed line was fitted to the oblique shock wave generated at the leading edge of the wedge model

Table 3 Post-oblique shock wave condition

	Hot gas condition	Cold gas condition
M_2	4.3	4.3
T_2 (K)	180	68
p_2 (kPa)	5.8	6.4
ρ_2 (kg/m^3)	0.11	0.33
u_2 (m/s)	1160	713
$Re_2 \times 10^6$ (1/m)	11	50

in Equation (1).

$$q_n = 2\sqrt{\frac{\rho_b c_b k_b}{\pi}}\sum_{i=2}^{n}\frac{T_i - T_{i-1}}{\sqrt{t_n - t_i} + \sqrt{t_n - t_{i-1}}} \tag{1}$$

, where ρ_b, c_b, and k_b are the density, specific heat at constant pressure, and thermal conductivity of the thermocouple. This equation indicates that all the temperature history is required to calculate the heat flux at a given time.

As mentioned earlier, the theoretical estimation of the heat flux at the stagnation point was performed based on the method proposed by Fay and Riddell [29] as shown in Equation (2).

$$q_s = 0.76\, Pr^{-0.6}(\rho_w \mu_w)^{0.1}(\rho_s \mu_s)^{0.4}\left\{1 + (Le^{0.52} - 1)\left(\frac{h_d}{h_s}\right)\right\}(h_s - h_w)\sqrt{\frac{du}{ds}} \tag{2}$$

, where *Pr* is the Prandtl number, *Le* is the Lewis number. Subscripts *w* and *s* denote values at the initial wall condition and the stagnation condition. The value h_d is associated with the energy of the gas dissociation and was set to zero in this study since the flow was considered to be chemically frozen. The final term shows the velocity gradient at the stagnation point as shown in Figure 6. For the modified Newtonian flow, the velocity gradient at the edge of the boundary layer along the blunt body is expressed as presented in Equation (3).

$$\frac{du}{ds} = \frac{1}{R}\sqrt{\frac{4}{Cp_{max}}\frac{(p_{02} - p_{\infty})}{\rho_s}} \tag{3}$$

, where R is the radius of the model, p_{02} is the total pressure at the stagnation point, and C_{pmax} is the pressure coefficient for the modified Newtonian theory. However, previous investigations [30, 31] showed that there occurs a huge discrepancy between the theoretically calculated value and experimentally obtained value of as much as 50% depending on how the velocity gradient is estimated. Irimpan and Menezes [32] improved the estimation of the velocity gradient and obtained a good agreement between the estimated and experimentally measured heat fluxes. The huge discrepancy between the heat fluxes seen in Figure 3 may be due to the insufficient approximation of the velocity gradient at the stagnation point on the hemisphere model. Additionally, the theory does not consider the time variation of the temperature of the wall. In this study, the initial wall temperature at the stagnation point for the cold gas condition cannot be determined because of the time variation of the freestream condition. The discrepancy in the stagnation heat flux may have become larger for the cold gas condition due to the difficulty in

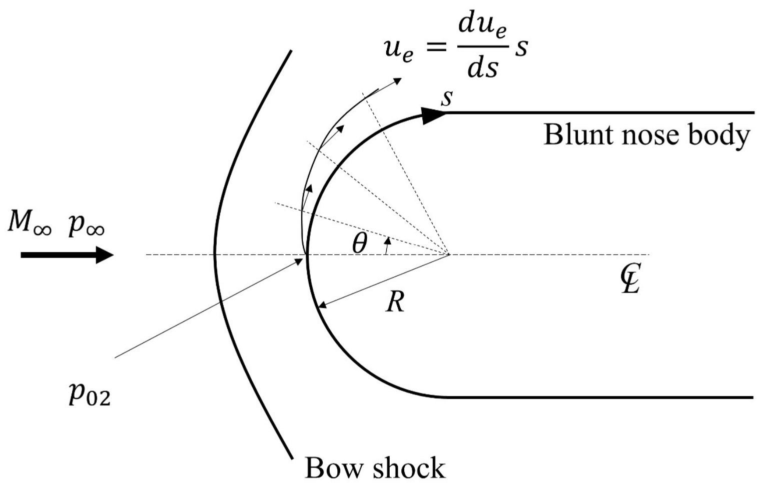

Figure 6 Schematic of the flow around a blunt nose body

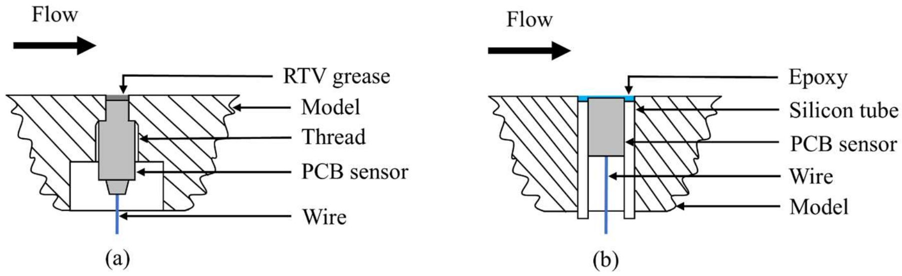

Figure 7 The schematic of sensor mounting on the wedge model. (a) Mounting of static pressure sensor and (b) mounting of pressure fluctuation sensor

determining the initial wall temperature.

2.3.2 Pressure Sensors

Three pressure sensors were directly mounted on the model to measure the static pressure and the pressure fluctuation as shown in Figure 7. For static pressure measurement, a PCB 105C02 was used. This pressure sensor had a measurement range of 690 kPa and a low- and high-frequency response of 0.5 Hz and 250 kHz. A small amount of RTV silicon grease was applied on the surface to protect the sensor from the heat during the tests. For pressure fluctuation measurement, two PCB 132B38 sensors were used. This pressure sensor was originally designed to capture a step-like pressure increment due to a shock wave arrival, but it was shown that the pressure sensor also could measure the high-frequency pressure fluctuation due to the instability waves in a boundary layer flow [33]. The low-frequency response was 11 kHz and the high-frequency response was 1MHz. A small amount of epoxy was applied on the surface of the sensors to make the sensors flush with the wedge surface. The pressure and thermocouple data were recorded at 2 MHz by the data acquisition system.

2.3.3 Temperature-Sensitive Paint (TSP)

To measure the temperature and heat flux distribution on the wedge, a Temperature-Sensitive Paint (TSP) was used. In this study, a binder-type TSP was used. The dichlorotris (1, 10-phenanthroline) ruthenium (II) hydrate was chosen as the luminescent molecule and a nylon-based polyamide was chosen as the binder to realize a high temperature sensitivity. The luminescent molecules and the binder were dissolved in ethanol. The TSP solution was applied to the surface of the WP layer with a spray gun following the manner in the previous works [27, 34]. The thickness of the TSP layer was estimated to be 3μm at maximum based on the amount of TSP solution. The thermal properties were taken from the previous study [27] to be; ρ_p=1.132×10^3 kg/m^3 ± 10%, c_p=2.07 kJ/kg-K ± 3%, α_p=0.84×10^{-7} m^2/s ± 7% for the TSP layer, and ρ_b=1.167×10^3 kg/m^3 ± 10%, c_b=1.59 kJ/kg-K ± 3%, α_b=1.09×10^{-7} m^2/s ± 7% for the WP layer, respectively. To excite the luminescent molecules two blue LED arrays with the dominant wavelength of 460 nm with a full width at half maximum (FWHM) of 20 nm were used. The emission light from the TSP layer was recorded by a high-speed camera equipped with an optical bandpass filter, that passed the light with wavelengths between 562.5 nm and 637.5 nm. The setting of the high-speed camera is presented in Table 4 and the schematic of the configuration of the TSP measurement is shown in Figure 8. The wedge model was located 50 mm downstream of the nozzle exit in the test section. To obtain the temperature information

Table 4 Camera settings for TSP measurements

	Low speed recording	High speed recordings	
Sampling frequency (kHz)	28.8	160	200
Image size (pixel)	608 × 896	96 × 896	112 × 512
Exposure (μs)	6.7	4.8	3.6
Resolution (mm/pixel)	0.24	0.22	0.21

from the recorded images, the calibration curve was used. The calibration was performed using a calibration chamber in which the temperature and the pressure could be controlled within 0.1K and 0.1 kPa. The calibration data was obtained before the wind tunnel experiments. The intensity information can be converted to temperature information via an empirical equation presented in Eqn (4) in general. The coefficients, a_i $(i = 0, 1, 2, \cdots, n)$, were determined by approximating the data point with an eighth-order polynomial in this study. The reference intensity was determined using a room temperature before each test. The calibration dat and the approximation are presented in Figure 9.

$$T = \sum_{i=0}^{n} a_i \left(\frac{I}{I_{ref}}\right)^i = a_0 + a_1 \left(\frac{I}{I_{ref}}\right)^1 + a_2 \left(\frac{I}{I_{ref}}\right)^2 + \cdots + a_n \left(\frac{I}{I_{ref}}\right)^n \quad (4)$$

The heat flux distribution was calculated from the temperature distribution similar to the TC, but for TSP measurement, the effect of the thickness of the TSP layer should be considered. For that purpose, the method proposed by Liu et al. [35] was implemented to calculate the heat

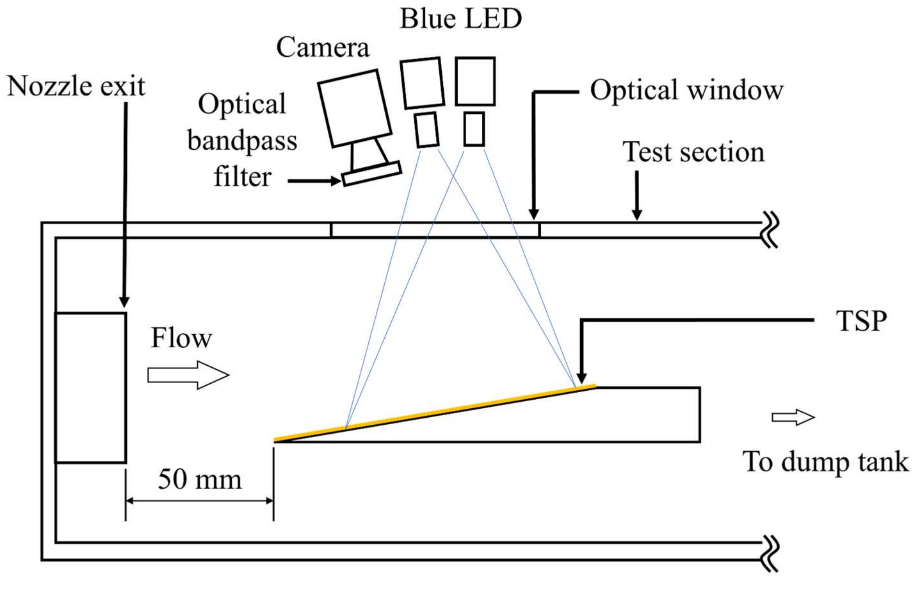

Figure 8 Schematic of TSP measurement configuration. Not to scale

flux distribution on the wedge. In the calculation of heat flux, the images were processed with smoothing filters to mitigate the noise. Firstly, the obtained images were normalized with a reference image to obtain the intensity ratio distribution. The intensity ratio distribution was processed with a 5-point moving average filter in the time direction. After converting to temperature distribution, the images were smoothed with a 15-point moving average temporal filter and a 5×5 spatial filter. The calculated heat flux distribution was smoothed with a 3-point temporal filter and a 5×5 spatial filter.

The uncertainty in the calculated heat flux strongly depends on the thermal properties of the TSP layer and base layer. The uncertainty of a TSP was discussed by Ozawa [27]. Because the same TSP and the base layer were used in this study, the uncertainty is considered to be similar.

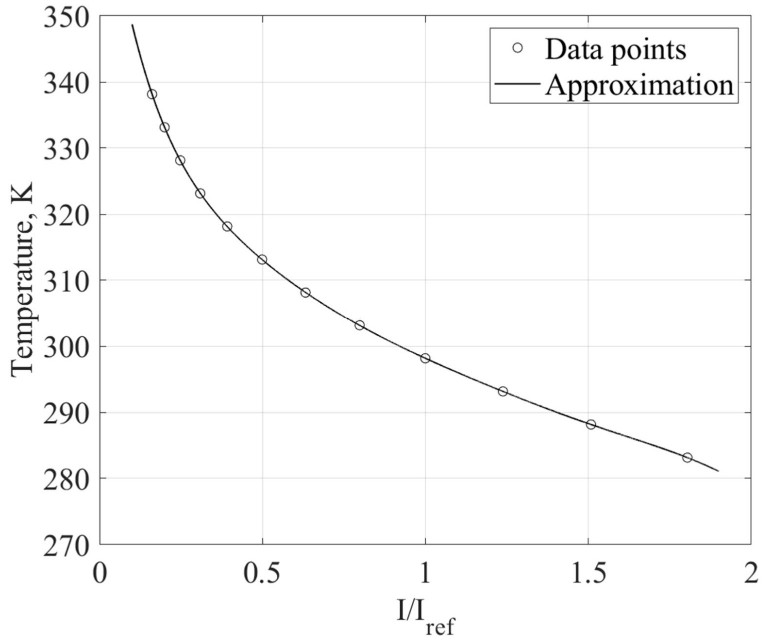

Figure 9 Calibration curve for TSP employed in this study

2.3.4 Schlieren Visualization

Schlieren visualization technique [36] was also used to visualize the flow around the wedge. A conventional Z-type Schlieren visualization was developed as a way to visualize the density gradient in the fluid, adding a knife edge to the shadowgraph technique. The schematic of the configuration of the Schlieren visualization used in this study is presented in Figure 10. The light source was a pulsed laser emitter. The synchronized laser emitter generated a series of laser pulses, and each pulse was turned on for 10 ns corresponding to the shutter opening. The light emitted from the light source made a focal point in front of the light source and an iris was used to make a point source of light. The light is reflected at the concave mirror to become an almost parallel beam. This light beam cannot be parallel since the point light source had a finite area, not a perfect "point" light source. The light beam passed through the test section was reflected by the second concave mirror and made another focal point, where a knife edge was applied horizontally to visualize the density gradient in the wall-normal direction. The

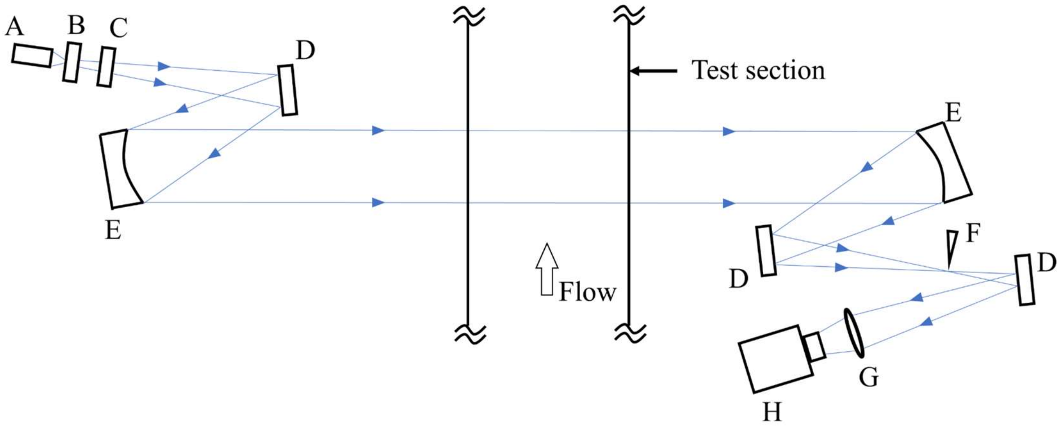

Figure 10 Schematic of the conventional Z-type Schlieren visualization system. Components are; A, Laser; B, Iris; C, N-D filter; D, Flat mirror; E, Concave mirror; F, Knife edge; G, Focusing lens; H, Camera

Schlieren images were recorded by the same high-speed camera that was used to make TSP measurements. In this study, the Schlieren visualization was mainly performed to obtain the oblique shock wave angle generated at the leading edge of the wedge and to check the freestream (see Figures 5 and 14).

3 Results and Discussion

3.1 Results from Pressure Sensors

From the pressure sensors mounted on the wedge model, the time history of pressure was obtained. In Fig. 11, the averaged time history of static pressure is shown together with the average values for the hot-, transitional, and cold gas conditions. The shot-to-shot deviations for each condition were calculated to be 6%, 3%, and 4%, respectively. The static pressure for the hot gas condition was higher by 47% than that presented in Table 3. The static pressure for the cold gas condition was also higher by 27% than that shown in Table 3. This discrepancy may have come from the curved shock wave due to the existence of the boundary layer on the wedge. Additionally, the pressure sensor was sensitive to structural vibration, which may have contaminated the pressure data.

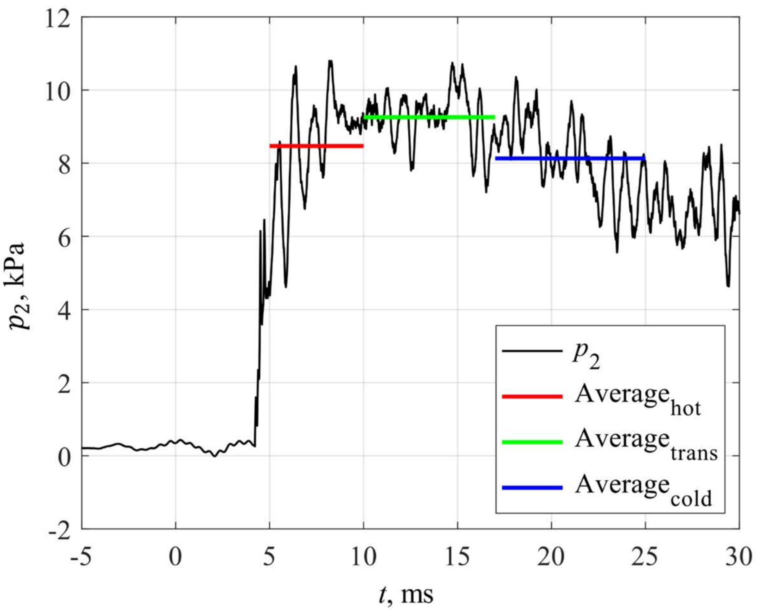

Figure 11 Averaged time history of static pressure at *x*=120 mm

Figure 12 shows the Power Spectral Densities (PSDs) estimated from the pressure records at x=100 and 180 mm. Since the Mach number at the edge of the boundary layer in this study was M_e=4.3, the dominant instability mode was expected to be the first mode, which typically has an order of 10^1 kHz [3, 33]. According to the manufacturer, the PCB138 sensor was high-pass filtered at 11 kHz. Additionally, the pressure sensor had noise due to the dynamics of the sensor at higher frequencies over 300 kHz [37]. For the above reasons, Figure 12 shows the frequency range between 10 kHz and 300 kHz. The mechanical oscillation of the wedge model and the impingement of the starting shock wave may have caused the energy concentration in the low-frequency region below f=30 kHz. In Figure 12(a), it is seen that the PSD at x=100 mm showed peaks at f=34 kHz, 51 kHz, and 71 kHz. Above 90 kHz there were no significant peaks in PSD except for a small peak at f=160 kHz. However, these peaks did not show a trend of frequency shift due to the change in the thickness of the boundary layer between hot- and cold gas conditions. Therefore, these peaks may not represent the modal phenomena. In Figure 12(b),

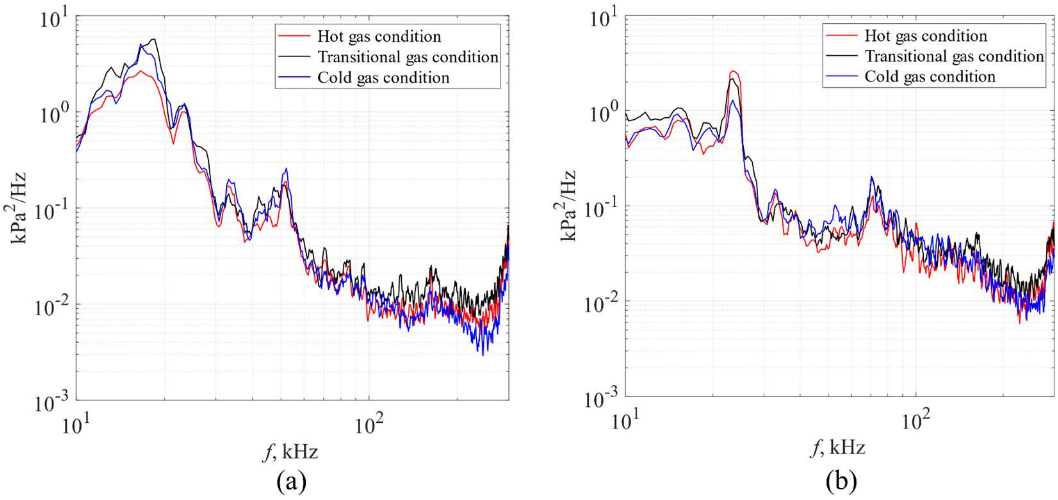

Figure 12 PSD estimates obtained (a) at x=100 mm and (b) at x=180 mm

the PSD at x=180 mm is presented. It is seen that there were some peaks at f=33 kHz and 71 kHz. Similar to the PSD at x=100 mm, those peaks may not represent the modal phenomena since they did not show a trend of frequency shift. However, the PSD at x=180 mm showed an enhanced signal in the magnitude between f=90 kHz and f=250 kHz. This may indicate that the boundary layer on the wedge was transitional and that the BLT started upstream of x=180 mm.

3.2 Results from TSP Measurements

In this section, the results obtained in the TSP measurements are presented. In the TSP measurements, the heat flux distribution on the wedge was obtained. As mentioned earlier, a low-speed recording with a large FOV was employed to observe the entire surface of the wedge. To track transient features such as turbulent spots, high-speed recordings were performed with narrow FOVs. First, the results for the hot-, cold-, and transitional gas conditions are presented in sections 3.2.1, 3.2.2, and 3.2.3, respectively, then the results are compared to each other in the section 3.2.4.

3.2.1 Hot Gas Condition

The time-averaged heat flux distribution obtained for the hot gas condition is shown in Figure 13. It is seen that there is a pair of waves impinging at the leading edge at y=±20 mm and the heat flux increased downstream of the impingement of the waves. These waves are considered to be generated inside the nozzle and were visualized in Schlieren visualization prior to the TSP measurements. The waves were so weak that they were barely seen in the Schlieren visualization until the knife edge was applied such that the intensity of the image became approximately 5% of that of the original image. The Schlieren image that was taken during a test before TSP measurements is shown in Figure 14 with the modified image for clarity. As a result of the impingement of the waves, the heat flux increased by 20~50% in the region of 20<|y|<60 mm compared to the region of |y|<20 mm. Therefore, in this study, it was assumed that the region of |y|<20 mm was not affected by the waves. Additionally, in Figure 13, it is seen that the heat flux near the acrylic plate on both sides increased significantly. The angle of the elevated heat flux region was approximately 3° and this was too small for the Mach angle in the Mach 5.2 flow. Hence, this is unlikely to be a shock wave phenomenon. Instead, this is considered to be due to the vortex generated in the corner floe region made by the wedge

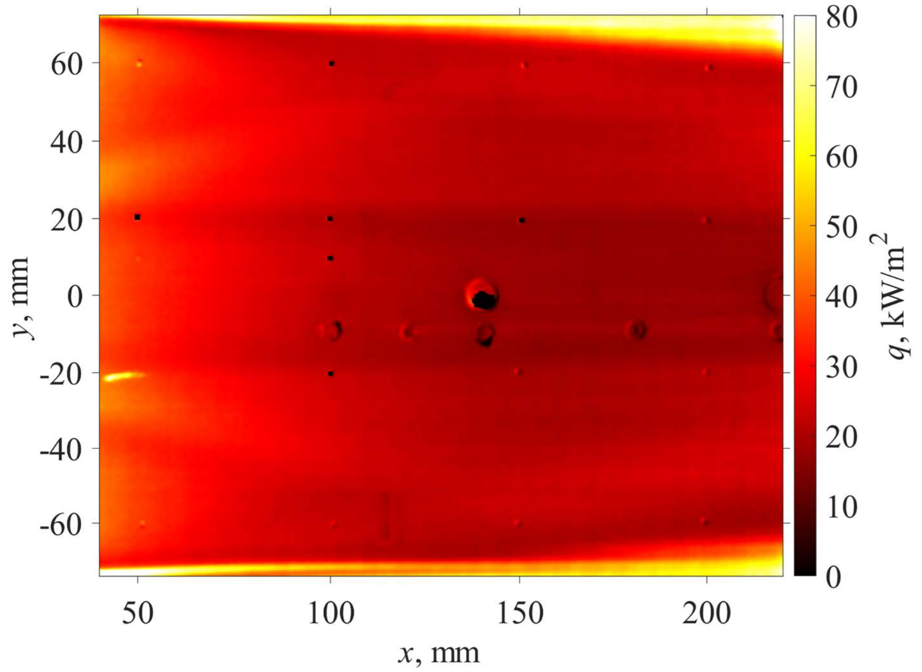

Figure 13 Time-averaged heat flux distribution on the wedge model for the hot gas condition

and the acrylic plates. The vortices in the corner flow promoted BLT near the acrylic plates and thus the heat flux in the region was elevated.

To observe the heat flux distribution in the streamwise direction, the heat flux distribution

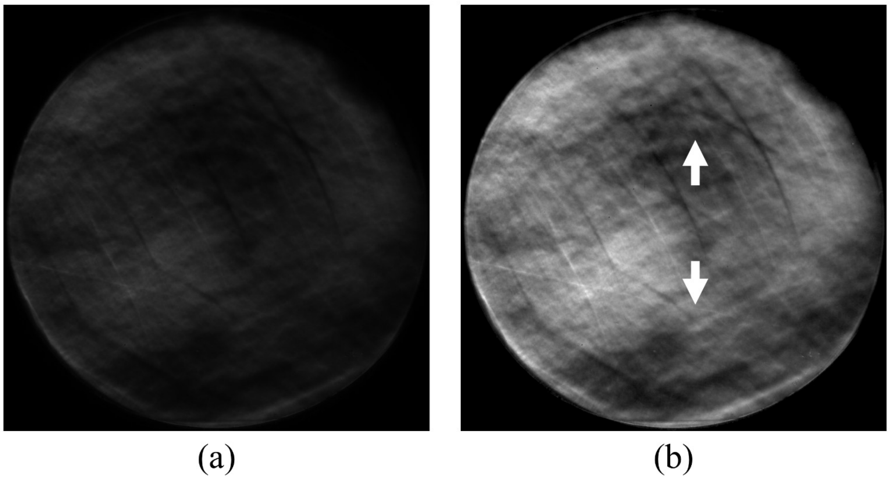

Figure 14 Schlieren images taken in a test duration. (a) The original image and (b) the modified image. Arrows point the weak waves

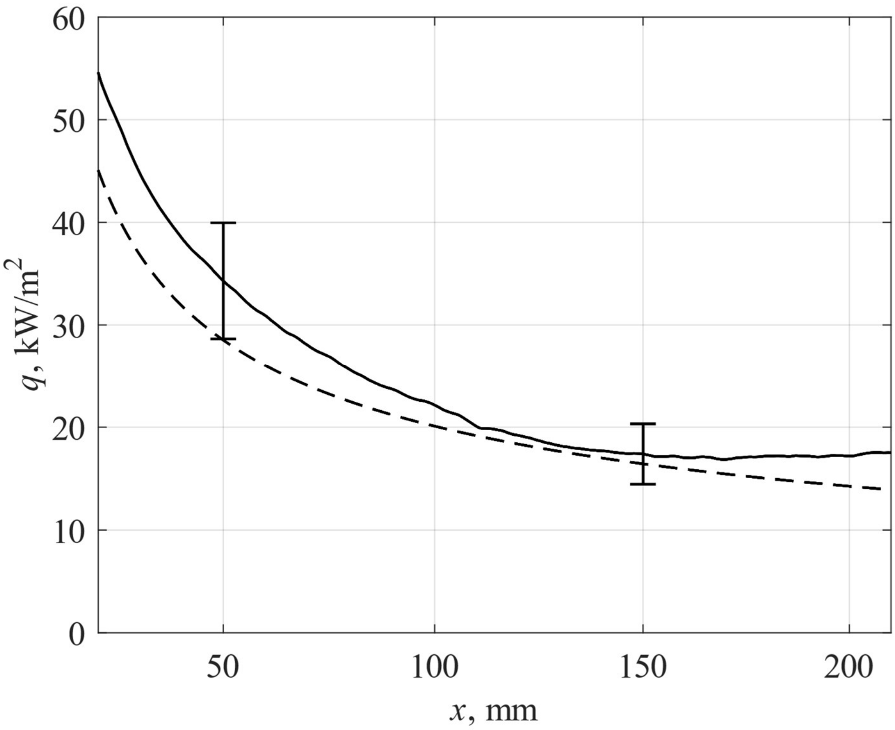

Figure 15 Heat flux distribution extracted at *y*=15mm from Figure 13. Solid line is for TSP-derived heat flux distribution; dashed line for the laminar estimate

at y=15 mm was extracted from Figure 13 and presented in Figure 15 together with the laminar heat flux distribution estimated by the Eckert reference temperature method [38, 39]. The theoretically estimated heat flux distribution decreases monotonically since it is proportional to the reciprocal of the distance from the leading edge, i. e., $q \propto \frac{1}{\sqrt{x}}$. The heat flux derived from TSP measurement also decreased monotonically as the distance from the leading edge increased and had a plateau of approximately q=17 kW/m^2 near x=160 mm. The TSP-derived heat flux distribution was in good agreement with theoretical estimation and did not show a trend of increasing downstream of the plateau, indicating that the boundary layer flow was

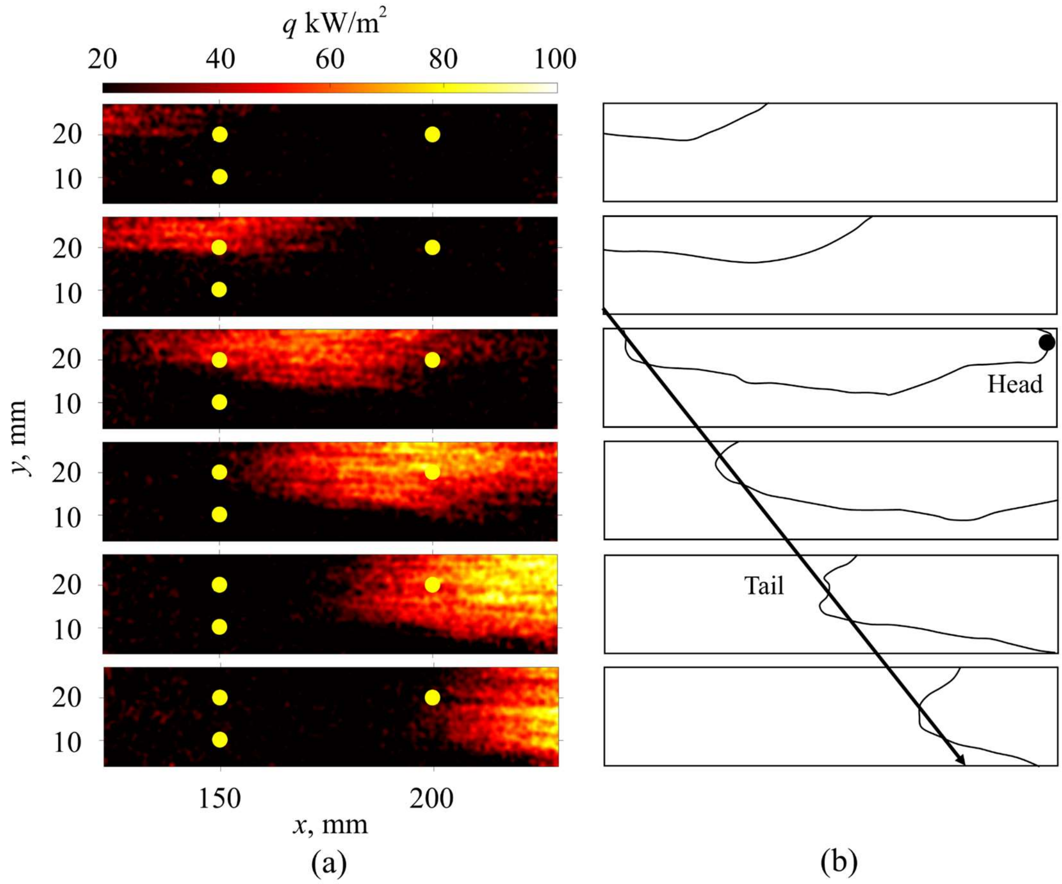

Figure 16 Time sequence of TS2. (a) TSP images and (b) sketches for each time. Yellow dots indicate the markers for reference of distance. Arrow indicates the trajectory of the tail of TS2. Black dot shows the head of TS2

laminar for the hot gas condition.

For the hot gas condition, three different turbulent spots, TS1, TS2, and TS3, were analyzed. The time sequence of TS2 is presented in Figure 16. Even though half of TS2 was not captured since TS2 appeared near the upper boundary of the FOV, the "footprint" of TS2 was clearly visualized. TS2 seemed to have propagated with a small angle to the centerline of the wedge model. The heat flux distribution beneath TS2 indicated that the heat flux was higher in the inner region of TS2. After the passage of TS2, the heat flux went back to the level that was observed before the appearance of TS2. Additionally, the streak-like pattern can be seen beneath TS2 associated with alternative high- and low heat flux in the spanwise direction. The distance between the streaks was measured to be λ=2.7±0.6 mm and did not vary during the propagation of TS2, while the number of the streaks increased downstream. This may indicate that the increase in the number of streaks resulted in an increase in the width of TS2.

To investigate the heat flux distribution beneath TS2, the heat flux distribution in the streamwise direction was extracted at y=24 mm, which is near the centerline of TS2. The heat flux distributions extracted at three different time instances are shown in Figure 17. It was seen that the peak of the heat flux was slightly upstream of the middle of the streamwise length of TS2. In the third time instance, the heat flux was below the reference laminar state just upstream of TS2. This indicated that there was a calm region, where turbulence was suppressed [18]. The peak of heat flux increased monotonically. At the earliest time instance, the peak of heat flux was q=48 kW/m^2 at x=141 mm. This is approximately 3.1 times the reference laminar state. At the latest time instance, the peak of heat flux increased to q=76 kW/m^2 at x=212 mm, corresponding to 5.1 times the reference laminar state.

For estimating the lateral spreading angle, the trajectories of points on either side that were

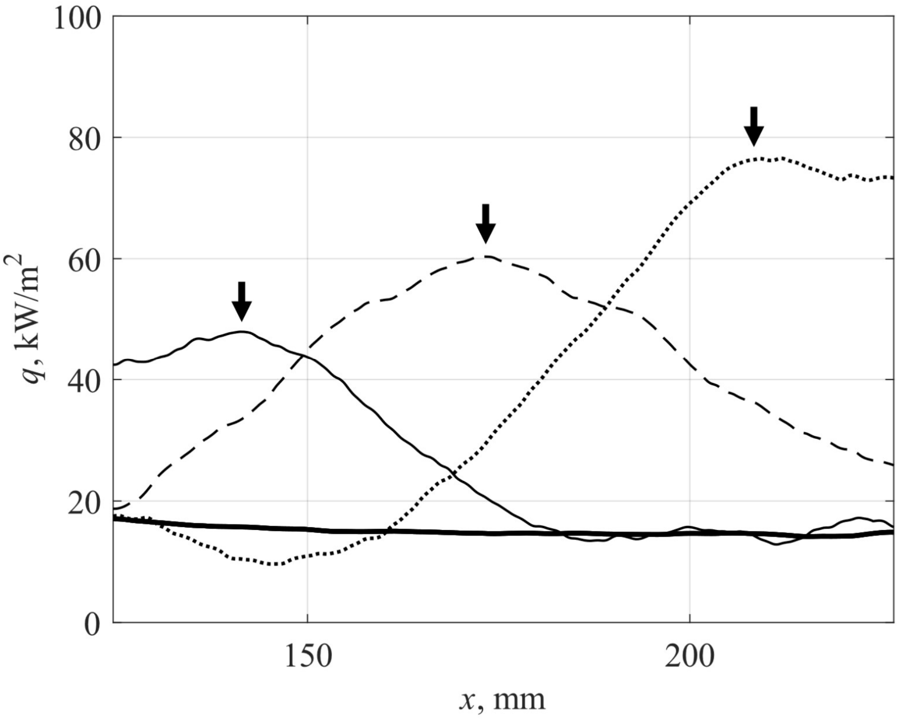

Figure 17 Heat flux distribution beneath TS2. The time step between each plot is 50 µs. Arrows indicate the peak of heat flux at each time instance

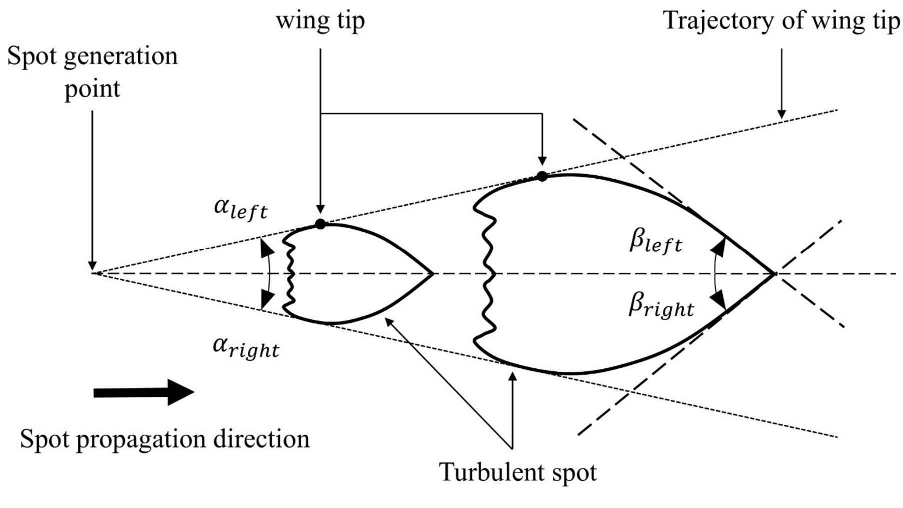

Figure 18 Schematic of a turbulent spot

the most distant from the centerline of a turbulent spot were investigated. Such a point was called the "wing tip" in previous research [14, 40]. In this study, the lateral spreading angle, α was measured from the line which is parallel to the centerline of the wedge. The definition of the lateral spreading angle is given in Figure 18 together with the schematic of a turbulent spot. For TS2, only α_{right} was measured since TS2 appeared at the upper boundary of the FOV. Figure 19 shows the image made by overlaying the time sequence of TS2. A line was fitted to the trajectory of a wing tip of TS2. At some points, such as x=157 mm and x=200 mm, the width of TS2 increased discontinuously due to the generation of additional streaks. Despite the discontinuous increment of the number of streaks, the width of TS2 showed a trend of increasing at a constant rate in general. The lateral spreading angle of TS2 was estimated to be α_{right}=8.3±1.5˚. However, this angle may be overestimated because TS2 seemed to propagate downstream with a slight angle regarding the centerline of the wedge as mentioned earlier. Similarly, the vertex angle, β_{right} was measured by fitting a line to the leading edge of TS2. The vertex angle of TS2 varied from β_{right}=15.0˚ to β_{right}=21.6˚. The vertex angle showed a trend of

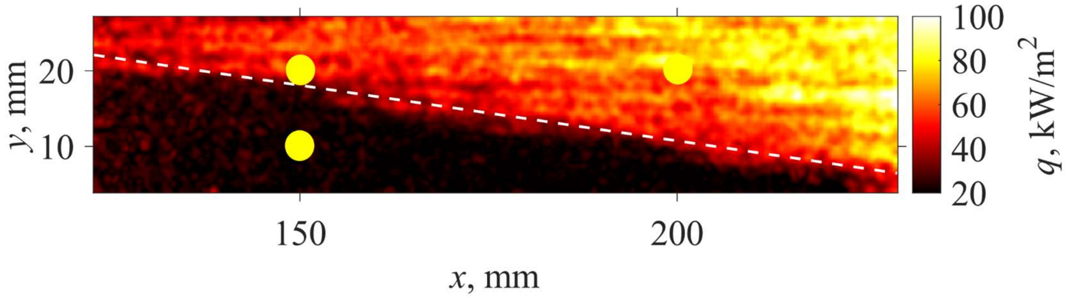

Figure 19 Overlaid image of TS2 obtained from the time sequence. Dashed line is fitted to the trajectory of the wing tip. Yellow dots indicate the markers for reference of distance

increasing just after TS2 appeared in the FOV, and later the vertex angle decreased when the head of TS2 appeared in the FOV. This is because the leading edge of TS2 was not a straight line, instead the angle was larger near the wing tip location (see third figures in Figure 16). As a result, the angle measured until the head of TS2 appeared might have been the angle of the steeper part of the leading edge.

To estimate the velocity at the head, v_h, peak heat flux point, v_q, and tail, v_t, of TS2, an *x-t* diagram was made from the time sequence. The time sequence of TS2 was nondimensionalized with the reference image, $q_{ref,\ hot}$ to highlight the variation of heat flux from the reference laminar state. To make the reference laminar state, TSP images that did not have transient features in them were averaged. The normalized heat flux distribution was extracted from y=24 mm and accumulated with respect to time. The *x-t* diagram for TS2 is shown in Fig. 20. The

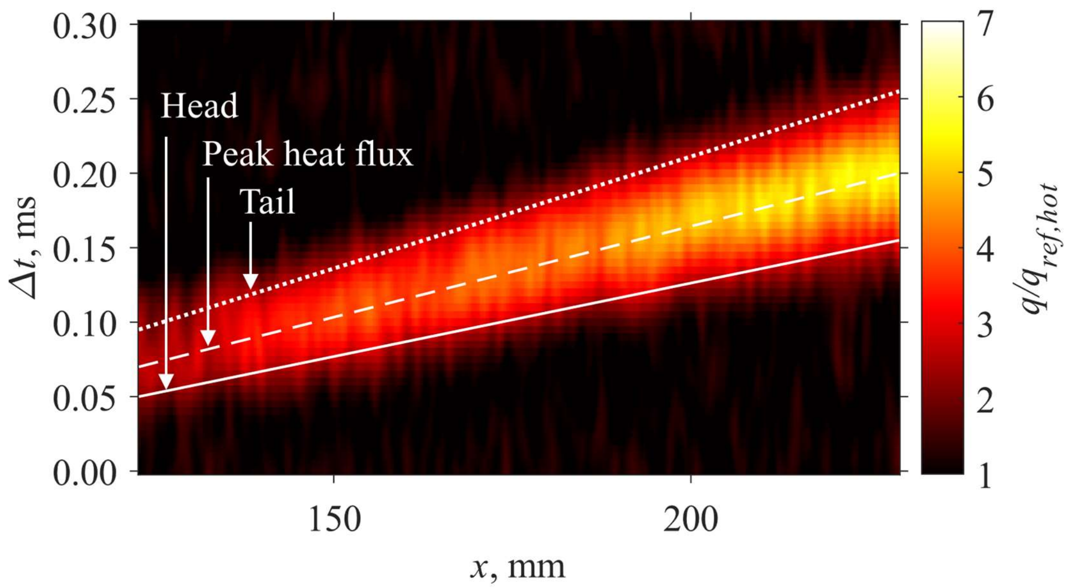

Figure 20 *x-t* diagram obtained from the time sequence of TS2. Solid line indicates the head; dashed line the peak heat flux point; dotted line the tail of TS2

passage of TS2 is depicted as a bright region from the bottom left to the top right. The trajectories of the head and tail of TS2 are depicted as the lower- and upper boundaries of the bright region. The velocities at the head and tail were estimated by fitting lines manually to the boundaries to be $v_{h,\ TS2}$=1010±160 and $v_{t,\ TS2}$ =670±100 m/s, respectively. The propagation velocities of a turbulent spot are often nondimensionalized with the boundary layer edge velocity, v_e, as $C_h= v_h/v_e$ and $C_t= v_t/v_e$. For TS2, the velocities were nondimensionalized by the boundary layer edge velocity, $v_{e,\ hot}$, to be $C_{h,\ TS2}$=0.87 and $C_{t,\ TS2}$=0.57. This means that the head and tail of TS2 propagated downstream at 87% and 57% of the boundary layer edge velocity for the hot gas condition. The velocity at the peak heat flux point of TS2 was estimated to be v_q=820±120 m/s using the same manner as for the head and tail of TS2. The velocity at the peak heat flux point was also nondimensionalized using the boundary edge velocity as $C_q=v_q/v_e$. The nondimensionalized velocity was C_q=0.70 for TS2.

3.2.2 Cold Gas Condition

The time-averaged heat flux distribution obtained for the cold gas condition is shown in Figure 21. The dynamic range was adjusted so that the feature on the surface of the wedge was visible. It is observed that some features observed for the hot gas condition were also seen such as the impingement of the weak waves and the elevated heat flux near the acrylic plates. The angle of the elevated heat flux region was slightly larger than that for the hot gas condition. The angle was measured to be approximately 5° and was still too small for the Mach angle for

M_∞=5.2 flow. Contrary to the hot gas condition, the heat flux showed a trend of increasing at the downstream region for the cold gas condition.

The heat flux distribution at y=15 mm was extracted from Figure 21 and presented in Figure 22 with the theoretical estimations. As mentioned earlier, the theoretically estimated heat flux distribution depends on the initial temperature at the wall. For the cold gas condition, the theoretical estimation of heat flux became negative when the initial wall temperature was assumed to be room temperature of T_w=300 K due to low temperature at the edge of the boundary layer, T_e=69 K. When the initial wall temperature was assumed to be T_w=150 K, the heat flux distributions agreed well to that obtained in the TSP measurements. This indicated that it was not adequate to assume the initial wall temperature for the cold gas condition to be the wall temperature before the wind tunnel starts for the theoretical estimation of heat flux

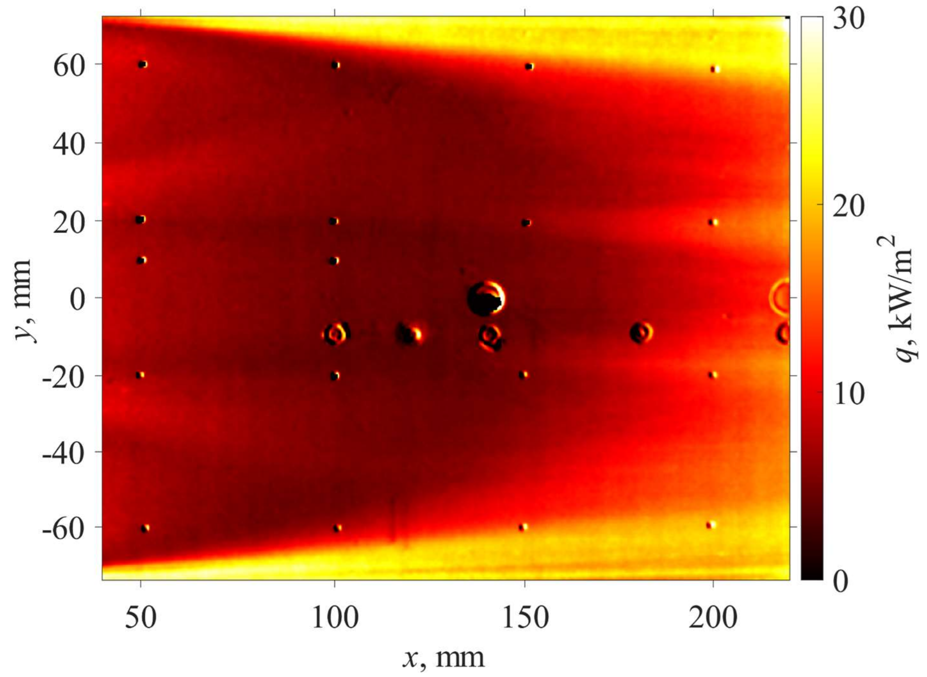

Figure 21 Time-averaged heat flux distribution on the wedge model for the cold gas condition

distribution for the cold gas condition. In Figure 22, it is seen that the TSP-derived heat flux kept decreasing and plateaued at q=4.2 kW/m^2 near x=130 mm. After the plateau, the heat flux started increasing near x=140 mm. When a boundary layer transitions from laminar to turbulent, small vortices are generated and the energy transport is enhanced between the surface and the fluid, as a result, the heat flux on the surface increases. Since the heat flux started increasing near x=140 mm, it was considered that the BLT started around this location. However, it is known that the location of the onset of BLT moves upstream and downstream over time [25]. To investigate the extent of the variation of the location of BLT onset, the heat flux distribution at y=15 mm at each time was extracted from the time sequence to determine the local minimum

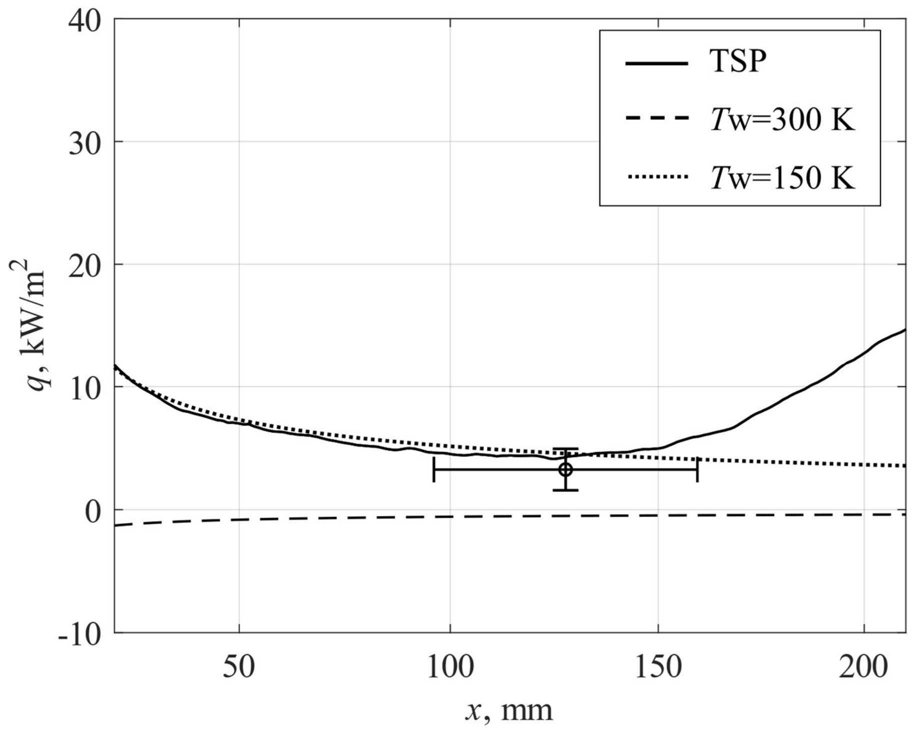

Figure 22 Heat flux distribution extracted at y=15 mm from Figure 21. The circle shows the average value of the local minimum of heat flux and the average distance that gave the local minimum of heat flux for cold gas condition. Dashed and dotted lines indicate laminar estimates

of heat flux and the streamwise location that gives the local minimum of heat flux. The circle in Figure 22 shows the average of the location that gives the local minimum of heat flux and the local minimum of heat flux. The vertical and horizontal bars show the standard deviation of those, showing that the onset of BLT moved from x=97 to 160 mm, and the local minimum of heat flux varied from q=1.6 to 4.9 kW/m^2.

For the cold gas condition, two different turbulent spots, TS4 and TS5, were analyzed. The time sequence of TS4 is shown in Figure 23 together with the sketches. TS4 seemed to have propagated with a slight angle to the centerline of the wedge. Because of the inclined path of TS4, the stretching in the spanwise direction was asymmetric. The right-hand side portion of TS4 when looked at from the upstream seemed to have a larger lateral spreading angle

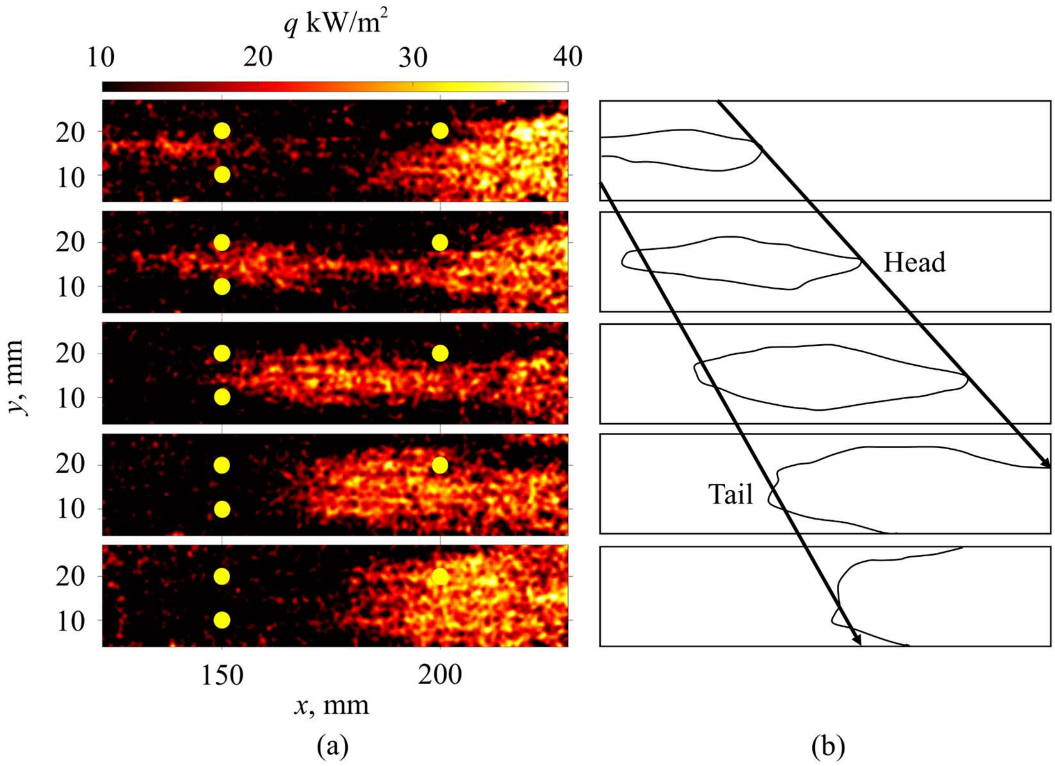

Figure 23 Time sequence of TS4. (a) TSP images and (b) sketches for each time. Yellow dots indicate the markers for reference of distance. Arrows indicate the trajectories of the head and tail of TS4

compared to the other side. TS4 seemed to have been generated near x=120 mm. In the first images in Figure 23, just after the generation, the tail of TS4 was triangular pointing upstream. In later time instances, the tail of TS4 caught up with the main body and gradually became flat. TS4 eventually merged with another high-heat flux region near x=190 mm. In the time sequence, the streak-like pattern associated with high- and low heat flux was faintly observed beneath TS4. The distance between the streaks was estimated to be λ=2.6±0.5 mm and did not vary during the propagation of TS4, while the number of streaks increased downstream.

Figure 24 shows the heat flux distribution beneath TS4 extracted from y=15 mm at three different time instances. The heat flux distribution was processed with a smoothing filter to observe the general trend. It is seen that the peak of heat flux was q=21 kW/m^2 near x=159 mm,

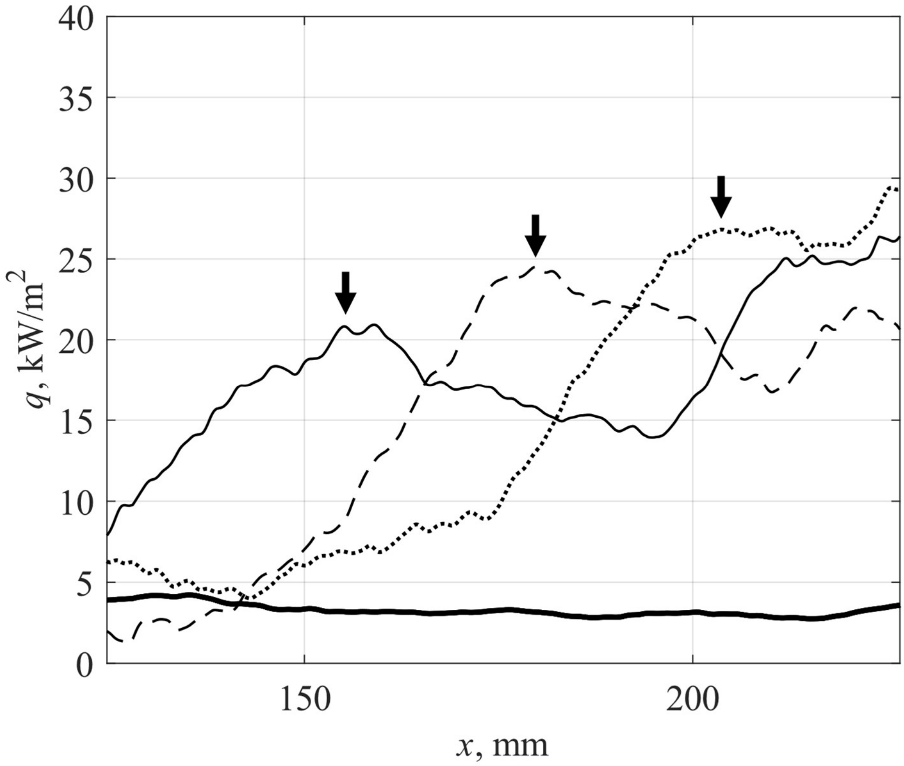

Figure 24 Heat flux distribution beneath TS4. The time step between each plot is 50 µs. Arrows indicate the peak of heat flux at each time instance

corresponding to 6.6 times the reference laminar state. At the latest time instance, it increased to q=27 kW/m^2 near x=205 mm, corresponding to 8.8 times the reference laminar state.

The lateral spreading angle of TS4 was estimated in the same manner as for TS2. The overlaid image of TS4 is presented in Figure 25. Since TS4 appeared near the center of the FOV, both trajectories of wing tips were able to be tracked. The trajectories seemed to have constant angles of α_{right}=9.1±3.6° and α_{left}=6.4±2.5°, respectively. The intersection of the fitted lines indicated that TS4 was generated near x=120 mm. The vertex angle of TS4 was also

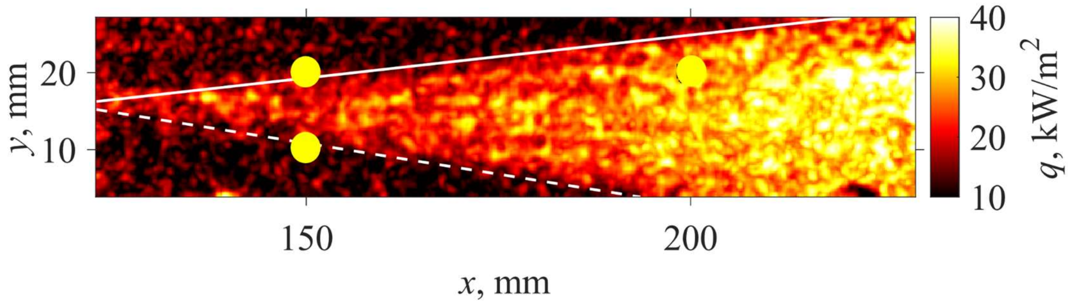

Figure 25 Overlaid image of TS4 obtained from the time sequence. Solid and dashed lines were fitted to the trajectories of the wing tips. Yellow dots indicate the markers for reference of distance

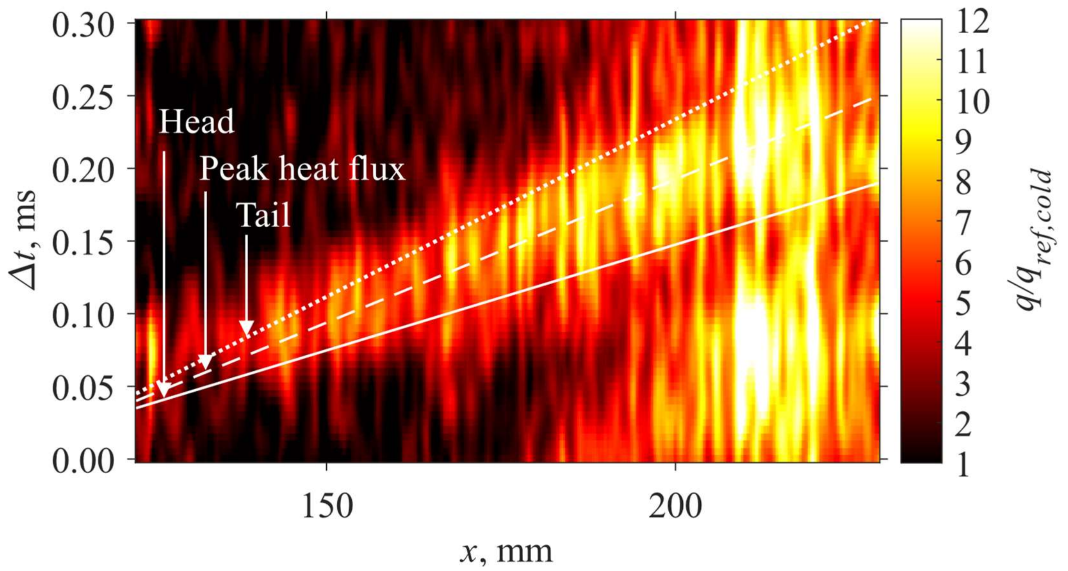

Figure 26 *x-t* diagram obtained from the time sequence of TS4. Solid line indicates the head; dashed line the peak heat flux point; dotted line the tail of TS4

measured. The vertex angles for both right- and left-hand sides (see Figure 18) showed a trend of increasing as TS4 propagated downstream. For TS4, the vertex angles varied from β_{right}=8.9° to β_{right}=11.0° and β_{left}=5.7° to β_{left}=8.5°.

To estimate v_h, v_q, and v_t, of TS4, an *x-t* diagram was made using the same manner as for TS2. The time sequence of TS4 was nondimensionalized using the reference image for the cold gas condition. The heat flux distribution was extracted at *y*=15 mm, which was near the centerline of TS4. The *x-t* diagram for TS4 is presented in Figure 26 together with the fitted lines to the trajectories of the head, peak heat flux, and tail of TS4. Although it was difficult to precisely measure the velocities at each location of turbulent spots for the cold gas condition due to the low signal-to-noise ratio, the velocities, v_h, v_q, and v_t were estimated from the *x-t* diagram to be $v_{h,\,TS4}$=690±260, $v_{q,\,TS4}$=510±190, and $v_{t,\,TS4}$=410±150 m/s with relatively large uncertainties. The corresponding nondimensional velocities were $C_{h,\,TS4}$=0.97, $C_{q,\,TS4}$=0.71, and $C_{t,\,TS4}$=0.57.

3.2.3 Transitional Gas Condition

For the transitional gas condition, the freestream condition, such as freestream temperature, density, and velocity, changed with time as mentioned earlier. This means that the "reference state" cannot be determined. Despite the fact, the reference laminar state for the transitional gas condition was defined as the average of the reference laminar states for the hot- and cold gas conditions in this study. In other words, to make the reference image for the transitional gas condition, the same number of TSP images were selected from both the hot- and cold gas conditions and then the images were averaged.

The time-averaged heat flux distribution for the transitional gas condition is presented in Figure 27. The dynamic range of heat flux was adjusted so that the features were visible. The time-averaged heat flux distribution was similar to that for the cold gas condition. However, the magnitude of heat flux was entirely higher than that for the cold gas condition. The heat flux profile at y=15 mm was extracted from Figure 27 and presented in Figure 28 together with those for the hot- and cold gas conditions for comparison. It is seen that the heat flux kept decreasing as the distance from the leading edge increased until x=130 mm, and then the heat flux began increasing. The time-averaged heat flux distribution for the transitional gas

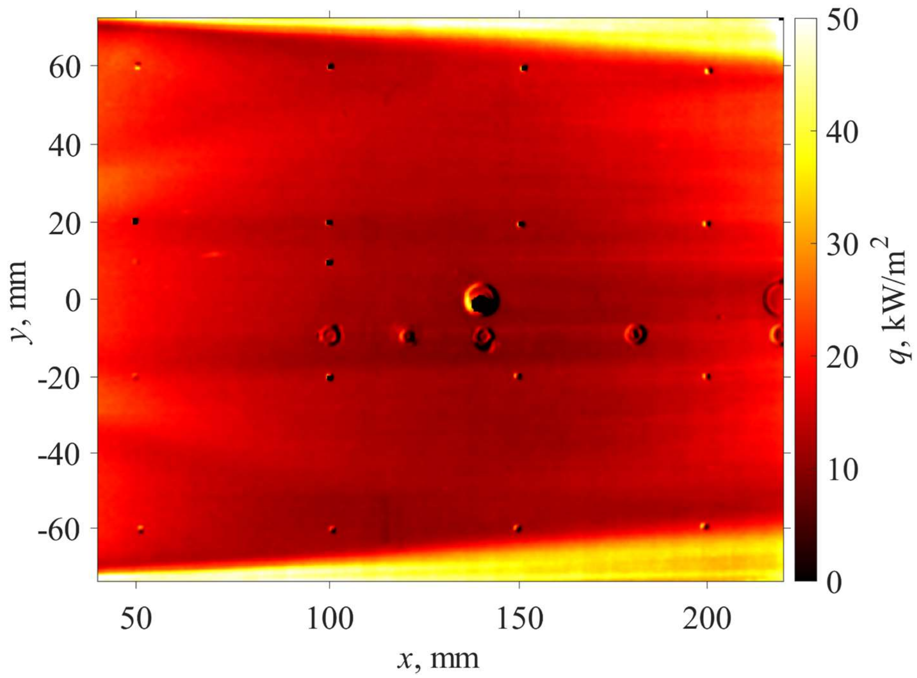

Figure 27 Time-averaged heat flux distribution on the wedge model for the transitional gas condition

condition was between those for the hot- and cold gas conditions until x=210 mm. Downstream of x=210 mm, the heat flux for the transitional gas condition may have exceeded that for the hot gas condition.

For the transitional gas condition, three different turbulent spots, named TS6, TS7, and TS8, were observed to be suitable for data analysis. Figure 29 shows the time sequence of the TS6 propagating downstream. It is seen that TS6 was generated near x=50 mm. Immediately after the generation, TS6 had a rhombus-like shape with vertices pointing upstream and downstream. In the first and second figures, the tail of TS6 remained at almost the same location and gradually propagated downstream to catch up with the main body of TS6. At later times the tail of TS6 began splitting and TS6 became the arrowhead shape eventually. The tail on the right-

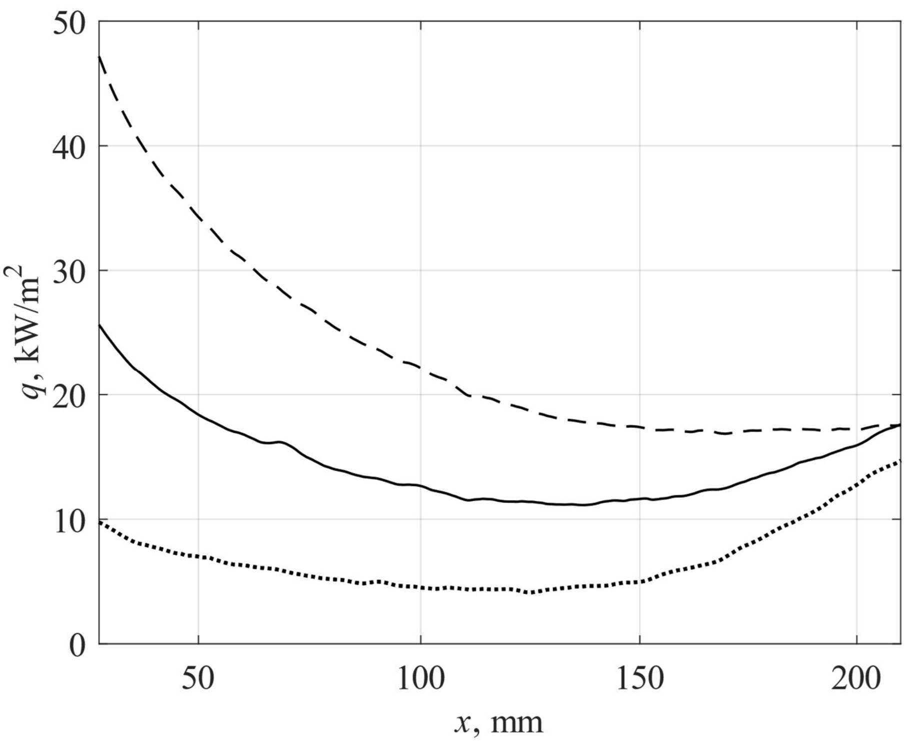

Figure 28 Heat flux distribution extracted at y=15 mm from Figure 27. Dashed line shows the time-averaged heat flux distribution for the hot gas condition; the dotted line for the cold gas condition

hand side of TS6 was longer compared to the one on the other side. During the propagation, TS6 stretched in the span- and streamwise directions, respectively, and the magnitude of the heat flux increased as TS6 propagated downstream. In addition to the generation and propagation, the streak-like pattern was also visualized in the time sequence of TS6. The distance between streaks was estimated to be λ=2.6±0.4 mm and almost unchanged during the propagation of TS6, while the number of streaks increased. TS6 showed the same trend that the increase in the number of streaks played a role in the lateral spreading. This trend was consistent for the hot-, cold-, and transitional gas conditions. It may be said that the distance between streaks was independent of the unit Re at the boundary layer edge, instead it was fixed by physical parameters such as surface roughness.

The heat flux distributions in the streamwise direction near the centerline of TS6 at four

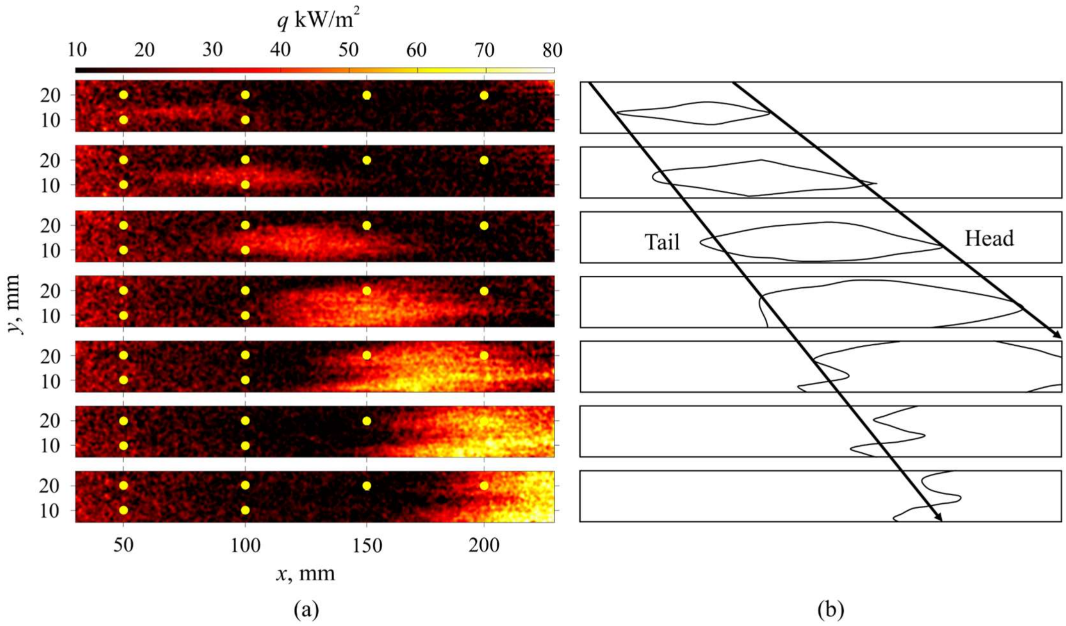

Figure 29 Time sequence of TS6. (a) TSP images and (b) sketches for each time. Yellow dots indicate the markers for reference of distance. Arrows indicate the trajectories of the head and tail of TS6

different time instances were presented in Figure 30 together with the reference laminar state for the transitional gas condition. It is seen that the peak of the heat flux increased at later time instances and the peak heat flux points were near the middle of the streamwise length of TS6. At the earliest time, the peak of heat flux was q=29 kW/m^2 near x=72 mm, corresponding to 1.9 times the reference state. At the latest time, the peak of heat flux increased to q=55 kW/m^2 near x=192 mm, corresponding to 5.6 times the reference state. The peak of the heat flux seemed to have increased monotonically as TS6 propagated downstream.

To measure the lateral spreading angle of TS6, TSP images were overlaid. The overlaid image of TS6 is presented in Figure 31. The heat flux distribution beneath TS6 was asymmetric regarding the centerline of TS6 due to the asymmetricity in its shape as mentioned earlier. Lines

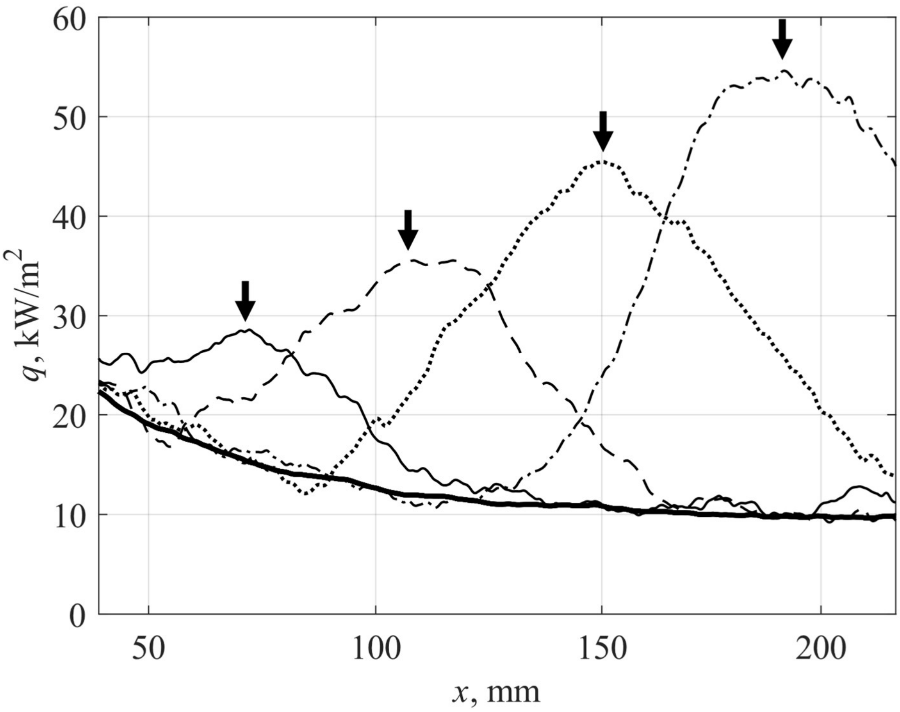

Figure 30 Heat flux distribution beneath TS6. The time step between each plot is 62.5 µs. Arrows indicate the peak of heat flux at each time instance

were fitted to the trajectories of the wing tips of TS6 and the lateral spreading angles were approximated to be α_{right}=5.1±0.9˚ and α_{left}=5.0±0.9˚, respectively. The vertex angle of TS6 was also measured from TSP images and showed a trend of increasing but the variation was smaller compared to those for TS2 and TS4. The variation of the vertex angle was from β_{right}=9.3˚ to β_{right}=12.5˚ and β_{left}=9.5˚ to β_{left}=11.3˚ for TS6.

For TS6, an *x-t* diagram was made using the same manner as for TS2 and TS4. The time sequence of TS6 was nondimensionalized using the reference image for the transitional gas condition, $q_{ref,\ trans}$. Here, the reference was defined to be the average of the reference state of

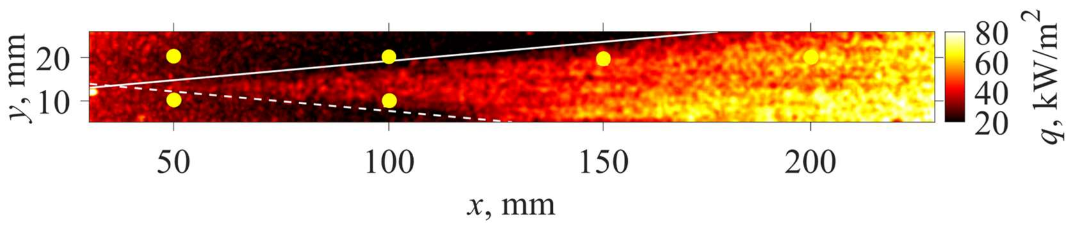

Figure 31 Overlaid image of TS6 obtained from the time sequence. Solid and dashed lines were fitted to the trajectories of the wing tips. Yellow dots indicate the markers for reference of distance

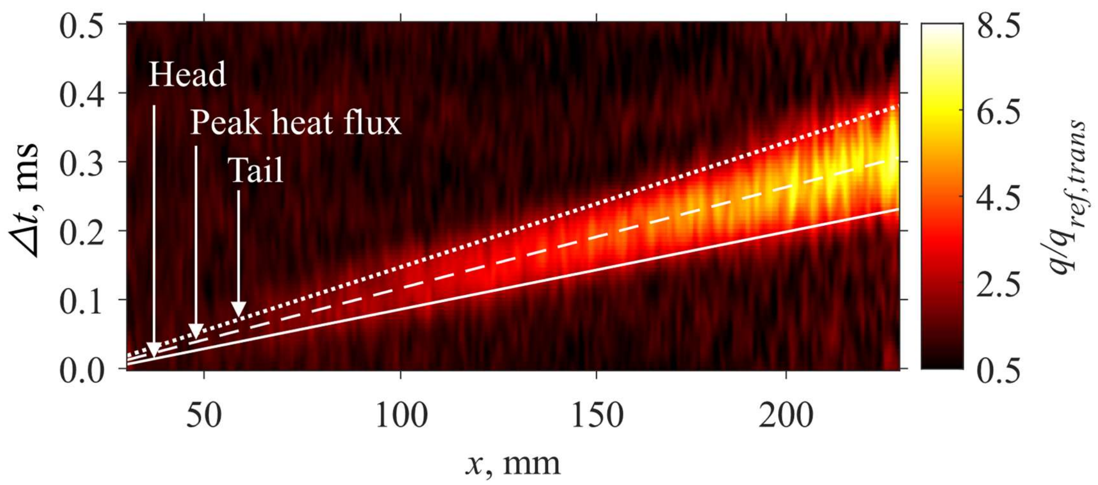

Figure 32 *x-t* diagram obtained from the time sequence of TS6. Solid line indicates the head; dashed line the peak heat flux point; dotted line the tail of TS6

the hot- and cold gas conditions as mentioned earlier. In the *x-t* diagram, the propagation of TS6 is clearly depicted. The peak heat flux point seemed to be in the middle of the streamwise length of TS6 as seen in Figure 32. The intersection of the lines indicated that TS6 was generated near x=30 mm, while the generation of TS6 seemed to be near x=50 mm in the time sequence. The propagation velocities v_h, v_q, and v_t, of TS6 were measured using the same manner as for TS2 and TS4 to be $v_{h,\,TS6}$=880±130, $v_{q,\,TS6}$=680±100, and $v_{t,\,TS6}$=550±80 m/s. The nondimensionalized velocities were calculated using the boundary layer edge velocity for the transitional gas condition $v_{e,\,trans}$. Here, $v_{e,\,trans}$ was defined to be the average of the edge velocities of the hot- and cold gas conditions, namely, $v_{e,\,trans}=0.5(v_{e,\,hot}+v_{e,\,cold})$. The nondimensionalized velocities for TS6 were then $C_{h,\,TS6}$=0.94, $C_{q,\,TS6}$=0.72, and $C_{t,\,TS6}$=0.59.

3.2.4 Comparison of Results for Each Condition

In this section, the comparisons of results obtained in the TSP measurements are presented and summarized.

First, the time-averaged heat flux distributions are normalized by the heat flux at the stagnation point in the test section for each condition, $q_{stag,\,hot}$ and $q_{stag,\,cold}$, for comparison. The normalized heat flux distributions are plotted against the local Re based on the distance from the leading edge, Re_x, in Figure 33 together with the instantaneous heat flux distribution beneath the turbulent spots observed for the hot- and cold gas conditions. Since the TSP images did not include the leading edge, Re_x started at Re_x=0.3×10^6. Although the same Re_x was obtained for both conditions between Re_x=1.4×10^6 and 2.4×10^6, the normalized heat flux distribution did not match each other. This discrepancy may have come from the uncertainty in the TC and TSP measurements. In this study, the temperature variation at the stagnation point in the test section was approximately 8 K during the test, resulting in the uncertainty in temperature of 21 % and thus it is considered that the heat flux at the stagnation point in the test section had an uncertainty on the same order. Regarding the TSP measurements, the derived heat flux might have been affected by the length of the test time. The test time from the beginning of the hot gas condition to the end of the cold gas condition was approximately 20 ms. Even though the thickness of the WP layer was assumed to be sufficient, the material of

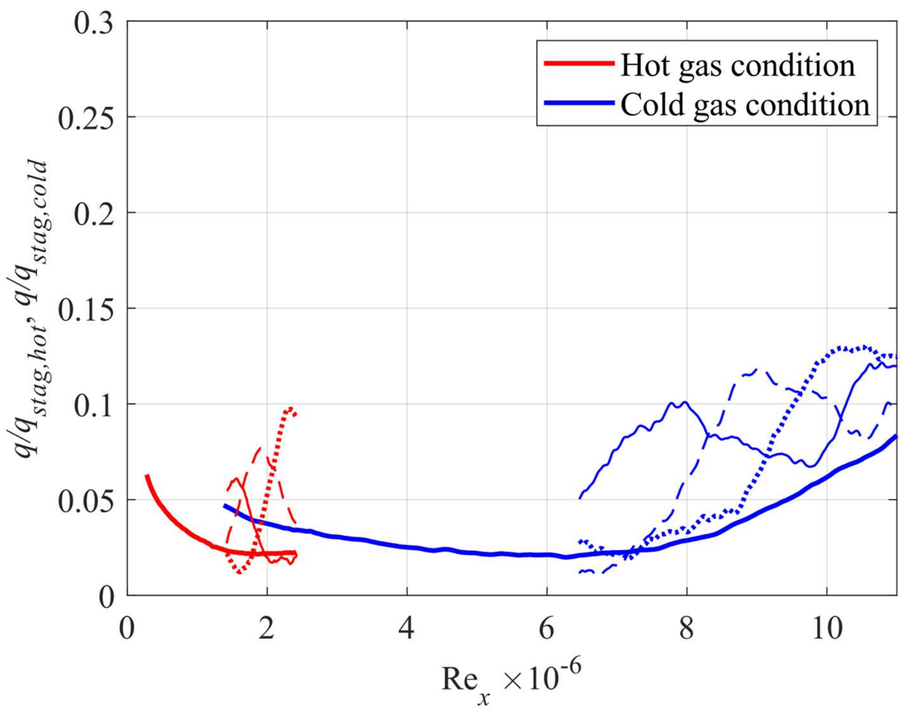

Figure 33 Nondimensional time-averaged heat flux distribution for hot- and cold gas conditions (thick lines) and nondimensional instantaneous heat flux distribution beneath TS2 and TS4 (thin lines)

the wedge and the change in thermal properties of the WP layer due to temperature change might have affected the temperature variation obtained from the TSP measurements and thus the derived heat flux.

Secondly, the propagating velocities for TS1 through TS8 are compared. Figure 34 shows the propagation velocity at the head, peak heat flux point, and tail of each turbulent spot and corresponding nondimensionalized velocities. In Figure 34(a), it is seen that v_h of turbulent spots for the hot gas condition was closely gathered near v_h≈1000 m/s, while v_h of turbulent spots for the cold gas condition was closely gathered near v_h≈700 m/s. The v_h of turbulent spots for the transitional gas condition varied from v_h=690 to 910 m/s to fall in between those for the hot- and cold gas conditions. v_q and v_t for each condition also showed the same trend. On the other hand, in Figure 34(b), it is seen that the nondimensionalized velocities were closely

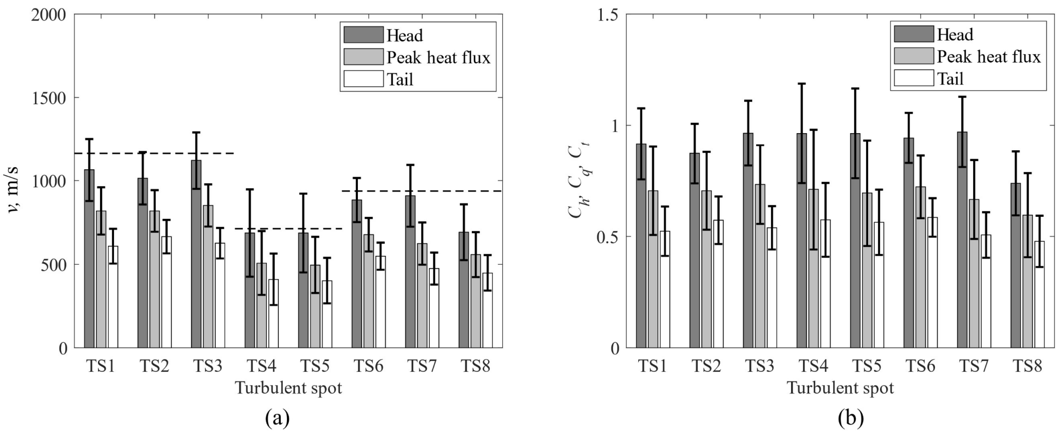

Figure 34 Velocities of TS1 through TS8. (a) Dimensional velocities measured at the head, peak heat flux point, and tail of turbulent spots and (b) corresponding nondimensional velocities. TS1 through TS3 were obtained for the hot gas condition, TS4 and TS5 for the cold gas condition, and TS6 through TS8 for the transitional gas condition. Dashed lines indicate the boundary layer edge velocities for each condition

gathered to each other for the hot- and cold gas conditions. C_h, C_q, and C_t for TS1 through TS5 were near 0.9, 0.7, and 0.6 respectively. However, C_h for TS8 was slightly smaller compared to the other turbulent spots. This discrepancy is because of the assumption of the boundary layer edge velocity for the transitional gas condition was not adequate for TS8. Again, for the transitional gas condition, it is not possible to determine the reference condition for normalization because the freestream condition changes with time. Noting the difficulty in the normalization of velocities for TS6 and TS7, this trend showed that the propagating velocity at the head, peak heat flux point, and tail of turbulent spots have constant fractions to the boundary layer edge velocity. These results are in good agreement with the previous investigations [11, 16]. Also, the results indicated that the freestream velocity changed during the transitional gas condition. The change in the freestream velocity is caused by the change in the temperature of the reservoir gas due to the contact surface arrival at the reservoir as mentioned earlier. When the contact surface arrives at the reservoir, the temperature in the reservoir decreases. The decrease in the reservoir temperature changes the freestream temperature, speed of sound, and thus velocity.

Third, the lateral spreading angle and the vertex angle are compared for each condition. Figure 35 shows the lateral spreading angle obtained for TS1 through TS8. It is seen that the lateral spreading angle was gathered between $\alpha=5^\circ$ and 10° regardless of the conditions in which the turbulent spots were observed. Even though the lateral spreading angles of the turbulent spots were similar to each other, they tended to be larger than the values collected by Fischer [40], which generally agreed with the theoretical estimation by Dooly and Smith [41]. Some previous works [10, 43] investigated the lateral spreading angle by measuring the fluid phenomena, such as velocity fluctuation using hot-wire anemometry. In this study, however, the lateral spreading angle was evaluated by measuring the surface heat transfer. Therefore, the discrepancy may occur due to the difference in the measurement techniques primarily. Noting the difference in the measurement technique, despite the M_e=4.3 in this study, the lateral spreading angle obtained was closer to those observed in low Mach number boundary layer flows than those in supersonic or hypersonic ones. James [21] investigated the lateral spreading angle of turbulent spots on free-flight objects in a gun tunnel using the shadowgraph technique. James observed α=11.8˚ under the M_e=3.9 environment but also mentioned that the result did

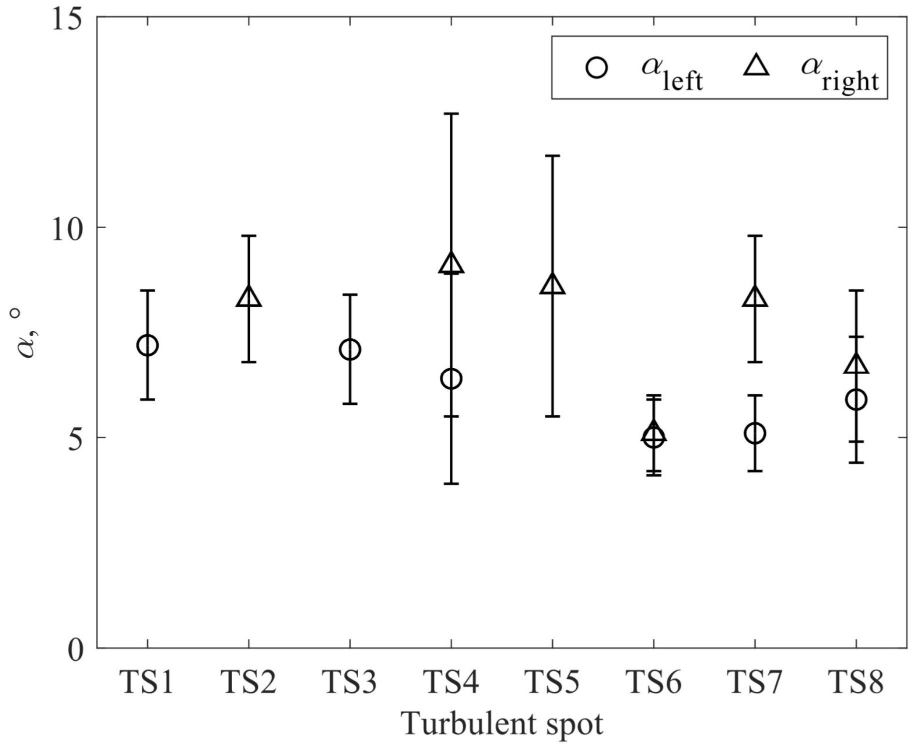

Figure 35 Lateral spreading angle for TS1 through TS8

not represent the general trend since it was observed in only one test.

For TS2, TS4, and TS5, the discrepancy in the lateral spreading angle may be due to the inclined path of the turbulent spots. In the time sequence, it was observed that some turbulent spots propagated downstream with an angle to the centerline of the wedge. This may be due to the three-dimensional effect. In this study, acrylic plates were attached on both sides of the wedge model, but the complete two-dimensional flow was not achieved. Hence, turbulent spots may have had a velocity component in the *y*-direction toward the centerline of the wedge, evidenced by the trend that the α_{right} is larger than or equal to the α_{left}. Although the investigations were done in low-speed environments, Clark et al. [44] and Chong and Zhong [40] studied the effect of pressure gradient on the lateral spreading angle of turbulent spots. They concluded that the lateral spreading angle decreased by the favorable pressure gradient. Chong and Zhong [40] also mentioned that the lateral spreading measured on the surface should be smaller than that measured above the surface since a turbulent spot has an overhang region.

Figure 36 shows the time variation of the vertex angle for TS1 through TS8. The vertex angles obtained in this study were between $\beta=5^\circ$ and $\beta=22^\circ$. Some of the available data regarding the vertex angle in previous studies are obtained in low-speed environments [10, 43, 45]. Amini and Lespinard [43] used hot-wire anemometry in low-speed wind tunnels and mentioned that the vertex angle of a turbulent spot is about $\beta=30^\circ$. Schubauer and Klebanoff [10] obtained the vertex angle of $\beta=15.3^\circ$ and also mentioned that the vertex angle was constant.

Gutmark and Blackwelder [45] used a thermocouple rake to observe the growth of turbulent spots on a flat plate and reported β=21˚-22˚ which showed good agreement with the flow visualization results by Gad-El-Hak et al. [14]. Additionally, similar values were obtained in high-speed flows by James [21] and Fiala et. al [16]. However, contrary to the observation of Schubauer and Klebanoff [10], the vertex angle showed a trend of increasing as turbulent spots propagated downstream. This may be due to the three-dimensional stretching of turbulent spots as mentioned by Fischer [41] and the interaction at the boundary between laminar and turbulent flows. Moreover, if a turbulent spot stretches conically inside a boundary layer as propagating downstream, the intersection between the conical growth of a turbulent spot and the surface may change shape and thus the vertex angle.

Finally, the global measurement of heat flux allowed to count the number of turbulent spots directly in the TSP images. Since it was expected that the turbulent spot generation rate was higher in the downstream region based on the time-averaged heat flux distribution (see Figures

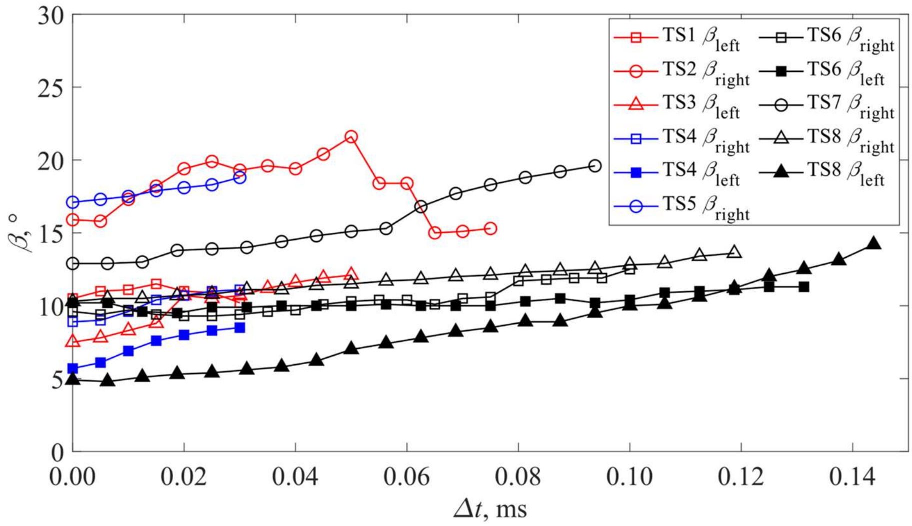

Figure 36 Time variation of the vertex angle for TS1 through TS8

22 and 28), the number of turbulent spots was counted at two streamwise locations, at x=150 mm and 200 mm. Figure 37 shows the number of turbulent spots observed and the estimated spot generation rate for the hot-, transitional-, and cold gas conditions, respectively. It is seen that the number of turbulent spots was much smaller for the hot gas condition compared to those for the other conditions, and for each condition, more turbulent spots were observed at x=200 mm than at x=150 mm. As mentioned earlier, turbulent spots are generated as a result of the breakdown of instability waves. In low-freestream disturbance environment, the disturbance is introduced to the boundary layer through the receptivity mechanism [8, 9] to generate instability waves. Instability waves are amplified as they propagate downstream and breakdown to turbulent spots when the amplitude exceeds the critical amplitude. For the hot gas condition, the amplitude of instability waves may have not reached the critical amplitude due to the low amplification rate based on the low unit Re. On the other hand, for the cold gas

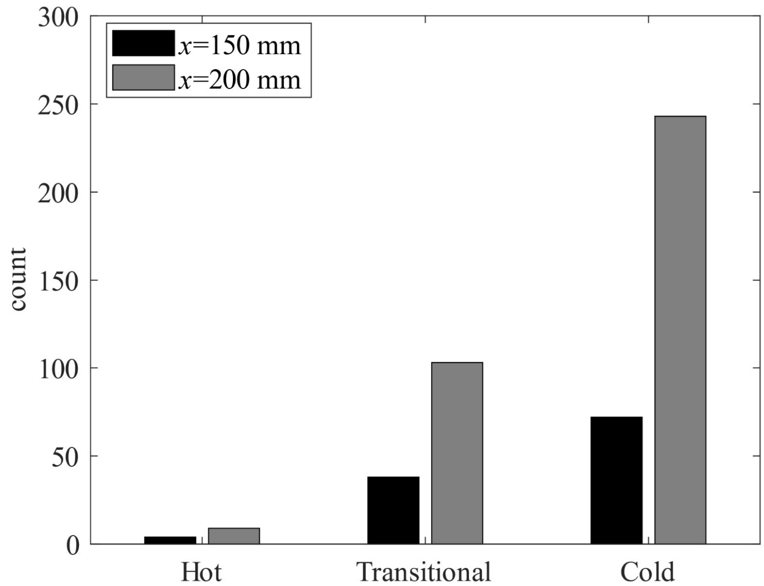

Figure 37 The number of turbulent spots observed for each condition

condition, the amplification rate was considered to be large enough for the instability waves to exceed the critical amplitude due to the large unit Re. The statistical observations of the number of turbulent spots may be done through the spot generation rate, n [48]. The spot generation rate shows the number of turbulent spots generated per unit width per unit time. Also, Mee and Tanguy [48] found a trend that the spot generation rate increased as the freestream unit Re increased. The trend in this study was in good agreement with the study by Mee and Tanguy [48]. Additionally, turbulent spots may be generated by directly receiving disturbances into the boundary layer such as an impingement of a small particle.

4 Concluding Remarks

4.1 Conclusion

In this study, the turbulent spots in hypersonic boundary layers were investigated and characterized by measuring the heat flux distribution on the wedge surface using a fast-response TSP. Additionally, pressure fluctuation was obtained from the pressure sensors mounted on the wedge model. The PSD obtained from the pressure records may have shown a trend that the boundary layer flow on the wedge was transitional based on the signal broadening. In the TSP measurements with a low sampling frequency, the time-averaged heat flux distribution was obtained and it showed that BLT started between approximately x=97 and 160 mm for the high unit Re condition. TSP measurements with high sampling frequencies were also carried out to track turbulent spots propagating in hypersonic boundary layers. The high-speed TSP measurements successfully visualized the “footprints” of turbulent spots with high spatial- and temporal resolutions for each unit Re condition. The propagation velocities at the head, peak heat flux point, and tail of turbulent spots were approximated to be 87-96%, 69-71%, and 52-57% of the boundary layer edge velocities regardless of the unit Re. These results are in good agreement with the results obtained in the previous investigations, showing the ability of the fast-response TSP to track the turbulent spots in hypersonic boundary layers. Moreover, global heat flux measurements allowed us to perform geometrical observations directly from the heat flux distribution. The lateral spreading angle and the vertex angle were measured from the TSP images to be α=5°-10° and β=5°-22°, respectively. The lateral spreading angle was larger than the previously reported data and close to the values obtained in low-speed experiments. The vertex angle showed a trend of increasing as turbulent spots propagated downstream. Additionally, those angles seemed to be less sensitive to the unit Re based on the comparison of results obtained for the low- and high-unit Re conditions. The number of turbulent spots was significantly higher for the high-unit Re condition compared to that for the low-unit Re condition.

4.2 Future Works

There are several options to improve and extend this study in the future. Firstly, it is necessary to consider the setting of TSP measurements. Due to the low signal-to-noise ratio, obtaining the instantaneous heat flux distribution on the order of 10^1 kW/m^2 was difficult, especially for the cold gas condition. This may be solved by increasing the intensity of the images. Additionally, improving the temperature sensitivity of the TSP is another option. There are several luminescent molecules used as a luminescent dye for TSP and also there are several choices for the binder. The proper combination of luminescent molecules and a binder may improve the temperature sensitivity of TSP [24].

Secondly, it is desirable for more test conditions to be added. In this study, only one test condition was employed to investigate the characteristics of turbulent spots. For example, the unit Re that were realized in this study were only Re_u=7.4×10^6 m^{-1} and 38×10^6 m^{-1} for the freestream conditions. Therefore, the characteristics, especially the lateral spreading angle and vertex angle observed in this study may have shown only limited trends. To achieve a wide range of unit Re in the freestream in the test section, one can change the initial conditions and/or replace the driver and driven gases of the shock tube section.

Lastly, simultaneous records of turbulent spots from different angles will reveal more details, since turbulent spots are three-dimensional turbulent structures. In this current study, only the information on the model surface was assessed in terms of the heat flux. Obviously, the results do not represent the whole characteristics of turbulent spots. Therefore, to understand the characteristics of turbulent spots three-dimensional observation is required.

References

[1] McKiernan G. R. and Schneider S. P., "Instability and Transition on a Cone with a Slice and Ramp at Mach 6," AIAA SciTech Forum, 11-15 & 19-21 January, 2021 DOI: 10.2514/6.2021-0249

[2] Wadhams T. P., Mundy E., MacLean M. G., and Holden S., "Ground Test Studies of the HIFiRE-1 Transition Experiment Part 1: Experimental Results," Journal of Spacecraft and Rockets, Vol. 45, No. 6, pp. 1134-1148, 2008 DOI: 10.2514/1.38338

[3] Kendal J. M., "Wind Tunnel Experiments Relating to Supersonic and Hypersonic Boundary-Layer Transition," AIAA Journal, Vol. 13, No. 3, pp. 290-299, 1975 DOI: 10.2514/3.49694

[4] Grossir G., Pinna F., Bonucci G., Regert T., Rambaud P., and Chazot O., "Hypersonic Boundary Layer Transition on a 7 Degree Half-Angle Cone at Mach 10," AIAA AVIATION Forum, 7th AIAA Theoretical Fluid Mechanics Conference, 16-20, June Atlanta, GA, 2014 DOI: 10.2514/6.2014-2779

[5] Mack L. M., "Linear Stability Theory and the Problem of Supersonic Boundary-Layer Transition," AIAA Journal, Vol. 1, No. 3, pp. 278-289, 1975 DOI: 10.2514/3.49693

[6] Sivasubramanian J. and Fasel H. F., "Direct Numerical Simulation of Transition in a Sharp Cone Boundary Layer at Mach 6: Fundamental Breakdown," Journal of Fluid Mechanics, Vol. 768, pp. 175-218, 2015 DOI: 10.1017/jfm.2014.678

[7] Egorov I. V., Fedorov A. V., and Soudakov V. G., "Receptivity of a Hypersonic Boundary Layer over a Flat Plate with a Porous Coating," Journal of Fluid Mechanics, Vol. 601, pp. 165-1187, 2008 DOI: 10.1017/S0022112008000669

[8] X. Zhong and X. Wang, "Direct Numerical Simulation on the Receptivity, Instability, and Transition of Hypersonic Boundary Layers," Annual Review of Fluid Mechanics, 44:527-61, 2012 DOI: 10.1146/annurev-fluid-120710-101208

[9] Fedorov A., "Transition and Stability of High-Speed Boundary Layers," Annual Review of Fluid Mechanics, 43:79-95, 2011 DOI: 10.1146/annurev-fluid-122109-160750

[10] Schubauer G. B. and Klebanoff P. S., "Contributions on the Mechanics of Boundary-Layer Transition," NACA Technical Note 3489, 1955

[11] Jewell J. S., Leyva I. A., and Shepherd J. E., "Turbulent Spots in Hypervelocity Flow," Experiments in Fluids, 58:32, 2017 DOI: 10.1007/s00348-017-2317-y

[12] Emmons H. W., "The Laminar-Turbulent Transition in a Boundary Layer," Journal of Aerospace Sciences, 18:490-498, 1951 DOI: 10.2514/8.2010

[13] Cantwell B., Coles D., and Dimotakis P., "Structure and Entrainment in the Plane of Symmetry of a Turbulent Spot," Journal of Fluid Mechanics, Vol. 87, Part 4, pp 641-672, 1978 DOI: 10.1017/S0022112078001809

[14] Gad-El-Hak M., Blackwelder R. F., and Rilley J. J., “On the Growth of Turbulent Regions in laminar Boundary Layers,” Journal of Fluid Mechanics, Vol. 110, pp. 73-95, 1981 DOI: 10.1017/S002211208100061X

[15] Mee D. J. and Goyne C. P., “Turbulent Spots in Boundary Layers in a Free-Piston Shock-Tunnel Flow,” Shock Waves, 6:337-343, 1996 DOI: 10.1007/BF02511324

[16] Fiala A., Hiller R., Mallinson S. G., and Wijesinghe H. S., “Heat Transfer Measurement of Turbulent Spots in a Hypersonic Blunt-Body Boundary Layer,” Journal of Fluid Mechanics, Vol. 555, pp. 81-111, 2006 DOI: 10.1017/S0022112006009396

[17] Mee D. J., Raghunath S., and McGilvray M., “Heat-Transfer Gauge Arrays for Identifying Spot Initiation in Hypersonic Transitional Boundary Layers,” Journal of Spacecraft and Rockets, Vol. 60 No. 5, 2023 DOI: 10.2514/1.A35662

[18] Jocksch A. and Kleiser L., “Growth of Turbulent Spots in High-Speed Boundary Layers on a Flat Plate,” International Journal of Heat and Fluid Flow, Vol. 29, Issue 6, pp. 1543-1557, 2008 DOI: 10.1016/j.ijheatfluidflow.2008.08.008

[19] Goldstein D., Chu J., and Brown G., “Lateral Spreading Mechanism of a Turbulent Spot and a Turbulent Wedge,” Flow Turbulence and Combustion, 98: 21-35, 2017 DOI: 10.1007/s10494-016-9748-z

[20] Demetriades A., “Hypersonic Viscous Flow over a Slender Cone Part III: Laminar Instability and Transition,” AIAA 7th Fluid and Plasma Dynamics Conference 17-19, June, Palo Alto, CA, 1974 10.2514/6.1974-535

[21] James C. S., “Observations of Turbulent-Burst Geometry and Growth in Supersonic Flow,” NACA Technical Note 4235, 1958

[22] Laurence S. J., Wagner A., and Hannemann. K., “Experimental Study of Second-Mode Instability Growth and Breakdown in a Hypersonic Boundary Layer Using High-Speed Schlieren Visualization,” Journal of Fluid Mechanics, Vol. 797, pp. 471-503, 2016 DOI: 10.1017/jfm.2016.280

[23] Butler C. S. and Laurence S. J., “Transitional Hypersonic Flow Over Slender Cone/Flare Geometries,” Journal of Fluid Mechanics, Vol. 949, A37, 2022 DOI: 10.1017/jfm.2022.769

[24] Liu T., Sullivan J. P., Asai K., Klein C., and Egami Y., “Pressure and Temperature Sensitive Paints,” Springer, 2021

[25] Ozawa H., Laurence S. J., Martinez Schramm J., Wagner A., And Hannemann K., “Fast-Response Temperature-Sensitive Paint Measurements on a Hypersonic Transition Cone,” Experiments in Fluids, 56:1853, 2015 DOI: 10.1007/s00348-014-1853-y

[26] Laurence S. J., Ozawa H., Martinez Schramm J. Butler C. S., and Hannemann K., “Heat-Flux Measurements on a Hypersonic Inlet Ramp Using Fast-Response

Temperature-Sensitive Paint," Experiments in Fluids, 60:70, 2019 DOI: 10.1007/s00348-019-2711-8

[27] Ozawa H., "Experimental Study of Unsteady Aerothermodynamic Phenomena on Shock-Tube Wall Using Fast-Response Temperature-Sensitive Paints," Physics of Fluids, 28, 046103, 2016 DOI: 10.1063/1.4947040

[28] Cook W. J. and Felderman E. J., "Reduction of Data from Thin-Film Heat-Transfer Gages: A Concise Numerical Technique," AIAA Journal, Vol. 4, No. 3, pp. 561-562, 1966 DOI: 10.2514/3.3486

[29] Fay J. A. and Riddell F. R., "Theory of Stagnation Point Heat Transfer in Dissociated Air," Journal of the Aeronautical Sciences, Vol. 25, Number 2, 1958 DOI: 10.2514/8.7517

[30] Oliveir H., "Influence of the Velocity Gradient on the Stagnation Point Heating in Hypersonic Flow," Shock Waves, Vol. 5, pp. 205-216, 1995 DOI: 10.1007/BF01419002

[31] Srinivasan K., Desikan S. L. N., Saravanan R., Kumar A., and Maurya P. K., "Fore-Body and Base Heat Flux Measurements on a Typical Crew Module in Short Duration Impulse Facilities," Applied Thermal Engineering, Vol. 103, pp. 842-854, 2016 DOI: 10.1016/j.applthermaleng.2016.04.111.

[32] Irimpan K. J. and Menezes V., "Stagnation Heat Flux Estimation in Spherically Blunt Axisymmetric Hypersonic Models," Proceedings of the Institution of Mechanical Engineers, Part G: Journal of Aerospace Engineering, 237(6), pp. 1369-1375, 2023 DOI: 10.1177/09544100221124799

[33] Flood J., Taubert L., and Craig S. A., "First and Mack-Mode Instabilities in a Flat-Plate Boundary Layer at Mach 4," AIAA SciTech Forum, 6-10, Orlando, FL, 2020 DOI: 10.2514/6.2020-0361

[34] Ozawa H. and Laurence S. J., "Experimental Investigation of the Shock-Induced Flow over a Wall-Mounted Cylinder," Journal of Fluid Mechanics, Vol. 849, pp. 1009-1042, 2018 DOI: 10.1017/jfm.2018.433

[35] Liu T., Cai Z., Lai J., Rubal J., and Sullivan J. P., "Analytical Method for Determining Heat Flux from Temperature-Sensitive-Paint Measurements in Hypersonic Tunnels," Journal of Thermodynamics and Heat Transfer, Vol. 24, No. 1, pp. 85-94, 2010 DOI: 10.2514/1.43372

[36] Settles G. S., "Schlieren and Shadowgraph Techniques: Visualizing Phenomena in Transparent Media," Springer, 2001

[37] Ort D. J. and Dosch J. J., "Influence of Mounting on the Accuracy of Piezoelectric Pressure Measurements for Hypersonic Boundary Layer Transition," AIAA SciTech Forum, 7-11, January San Diego CA, 2019 DOI: 10.2514/6.2019-2292

[38] White F. M., "Viscous Fluid Flow 2nd Edition," McGraw-Hill, 1991

[39] Eckert E. R. G., "Engineering Relations for Heat Transfer and Friction in High-Velocity Laminar and Turbulent Boundary-Layer Flow over Surfaces with Constant Pressure and Temperature," Journal of Fluids Engineering, Vol. 78, Issue 6, 1956 DOI: 10.1115/1.4014011

[40] Chong T. P. and Zhong S., "On the Three-Dimensional Structure of Turbulent Spots," Journal of Turbomachinery, Vol. 127, pp. 545-551, 2005 DOI: 10.1115/1.1928286

[41] Fischer M. C., "Spreading of a Turbulent Disturbance," AIAA Journal, Vol. 10, No. 7, pp. 952-953, 1972 DOI: 10.2514/3.50265

[42] Doorly D. J. and Smith F. T., "Initial-Value Problems for Spot Disturbances in Incompressible or Compressible Boundary Layers," Journal of Engineering Mathematics, 26:87-106, 1992 DOI: 10.1007/978-94-011-2440-9_8

[43] Amini J. and Lespinard G., "Experimental Study of an "Incipient Spot" in a Transitional Boundary Layer," Physics of Fluids, 25, 1743-1750, 1982 DOI: 10.1063/1.863651

[44] Clark J. P., Jones T. V., and LaGraff J. E., "On the Propagation of Naturally-Occurring Turbulent Spots," Journal of Engineering Mathematics 28: 1-19, 1994 DOI: 10.1007/BF02383602

[45] Gutmark E. and Blackwelder R. F., "On the Structure of a Turbulent Spot in a Heated laminar Boundary Layer," Experiments in Fluids, 5:217-229, 1987 DOI: 10.1007/BF00279733

[48] Mee D. J. and Tanguy G., "Turbulent spot Initiation Rates in Boundary Layers in a Shock Tunnel," 29th International Symposium on Shock Waves 1, 2015 DOI: 10.1007/978-3-319-16835-7_99